Martensitic twinning transformation mechanism in a metastable IVB element-based body-centered cubic high-entropy alloy with high strength and high work hardening rate

Yuhe Huang [a,b], Junheng Gao [a,c,*], Vassili Vorontsov [d], Dikai Guan [a], Russell Goodall [a], David Dye [d], Shuize Wang [c], Qiang Zhu [b], W.Mark Rainforth [a], Iain Todd [a]

[a]Department of Materials Science and Engineering, University of Sheffield, Sheffield, S1 3JD, UK

[b]Department of Mechanical and Energy Engineering, Southern University of Science and Technology, Shenzhen, 518055, China

[c]Beijing Advanced Innovation Center for Materials Genome Engineering, University of Science and Technology Beijing, Beijing 100083, China

[d]Department of Materials, Royal School of Mines, Imperial College London, London SW7 2BP, UK

Abstract

Realizing high work hardening and thus elevated strength–ductility synergy are prerequisites for the practical usage of body-centered-cubic high entropy alloys (BCC-HEAs). In this study, we report a novel dynamic strengthening mechanism, martensitic twinning transformation mechanism in a metastable refractory element-based BCC-HEA $(TiZrHf)_{87}Ta_{13}$ (at.%) that can profoundly enhance the work hardening capability, leading to a large uniform ductility and high strength simultaneously. Different from conventional transformation induced plasticity (TRIP) and twinning induced plasticity (TWIP) strengthening mechanisms, the martensitic twinning transformation strengthening mechanism combines the best characteristics of both TRIP and TWIP strengthening mechanisms, which greatly alleviates the strength-ductility trade-off that ubiquitously observed in BCC structural alloys. Microstructure characterization, carried out using XRD and EBSD shows that, upon

straining, α" (orthorhombic) martensite transformation, self-accommodation (SA) α"

twinning and mechanical α" twinning were activated sequentially. TEM analyses

reveal that continuous twinning activation is inherited from nucleating mechanical

$\{351\}_{\alpha"}$ type I twins within SA "$\{351\}$"$<\bar{2}11>_{\alpha"}$ type II twinned α" variants on $\{351\}_{\alpha"}$

twinning plane by twinning transformation through simple shear, thereby

accommodating the excessive plastic strain through the twinning shear while

concurrently refining the grain structure. Consequently, consistently high work

hardening rates of 2-12.5 GPa were achieved during the entire plastic deformation,

leading to a high tensile strength of 1.3 GPa and uniform elongation of 24%. Alloy

development guidelines for activating such martensitic twinning transformation

strengthening mechanism were proposed, which could be important in developing

new BCC-HEAs with optimal mechanical performance.

Keywords: Metastable high entropy alloy; Work hardening rate; Martensitic

transformation; Self-accommodating martensite; Twinning transformation

1. Introduction

High entropy alloys (HEAs) consisting of multiple constituent elements with

near-equimolar fractions have attracted significant interest due to their excellent

mechanical performance at both ambient and elevated temperatures[1–5]. The high

configurational entropy of HEAs intrinsically enhances the thermal stability of solid

solution phases at high-temperature. This is particularly evident in a group of body-

centered-cubic (BCC) HEAs, which primarily consists of group IV, V and VI refractory

transition elements[6–14]. Exhibiting high strength, high thermal softening resistance and microstructural stability up to 1600 ℃, these refractory element-based BCC-HEAs possess desirable characteristics for operating in the extremely high-temperature range, where conventional Co and Ni-based superalloys cannot be employed due to relatively low melting points[15,16]. However, due to the nature of the BCC structure (i.e., not a close-packed structure) and the lack of strengthening mechanisms, most of the refractory BCC-HEAs exhibit a low work hardening response and poor uniform ductility at ambient temperature[17–20], preventing their widespread usage.

Deformation-induced martensite phase transformation is an effective approach to alleviate the strength-ductility trade-off in metallic materials, e.g., high-Mn steels[21–23] and metastable BCC β-Ti alloys[24–28]. The phase transformation resulted in a dynamic strengthening effect, greatly enhancing the work hardening capability, thereby enabling high strength and large uniform elongation simultaneously[24,28,29]. Such a phenomenon is known as transformation induced plasticity (TRIP) and has been successfully applied to BCC-HEAs through metastable engineering which exhibit the stress-induced β to α (hexagonal close-packed)[30], β to α''(orthorhombic)[31–33] and β to α'' to α phase transformation[34]. Nevertheless, in some cases, the TRIP effect alone is insufficient to maintain a high work-hardening capability over the entire deformation duration, leading to the occurrence of plastic instability (necking) at early strain levels. For instance, owing to the inconsistent work hardening capability, for some TRIP Ti alloys with stress-induced α'' as dominant deformation mechanisms, high work hardening rate was

only observed during early deformation duration, thus resulting in a low fracture strength of ~300-600 MPa or limited elongation of ~10%[35,36]. To address this issue, in face-centered-cubic (FCC) alloys, concurrent TRIP and twinning-induced plasticity (TWIP) effects in the primary phase have been shown to be an efficient route to realize consistently high work hardening response[37–39]. Moreover, different from the conventional TRIP and TWIP mechanisms in primary austenitic phases of steels and Ti alloys, Li et al.[40] reported that TWIP effect can be introduced into the mechanically induced martensite of a metastable Fe-Mn-based HEA. It provided an assisted strengthening mechanism to TRIP and played a decisive role in maintaining continuously high work hardening response due to the high-density interfaces that arise from both phase transformation and consistently generated martensitic mechanical twins during deformation. However, similar TWIP effect in the mechanically induced martensite has seldomly been reported in metastable BCC-HEAs. Although twinning has been observed in martensite of metastable BCC-HEAs such as the $\{10\bar{1}1\}_{hcp}$ twinning in as-cast TiZrHfTa0.4[23] and $\{111\}_{\alpha''}$ type I twinning in Ti48Zr20Hf15Al10Nb7[25], different from mechanical twinning, these twinning are generally formed by transformation strain during phase transformation instead of structural shear in plastic deformation[30,41].

Here, we report that combined TRIP and extensive martensitic TWIP effect can be coherently achieved in thermomechanical treated metastable TiZrHfTa RHEAs through a specific martensitic twinning transformation mechanism. To optimize the martensitic twinning transformation, we systematically studied the effect of phase stability by intentionally varying the amount of β-stabilizer, Ta. Owing to their

outstanding mechanical performances, in this work, we concentrate on the study of (TiZrHf)$_{85}$Ta$_{15}$ and (TiZrHf)$_{87}$Ta$_{13}$ alloys (in atomic percentage, at.%), hereafter referred to as Ta15 and Ta13, respectively. Multiple deformation mechanisms including stress-induced martensite, antiphase boundary (APB)-like stacking fault, self-accommodation (SA) twinning (also known as transformation twinning) that used to accommodate the overall volume change between the martensite and austenite phases[41–43], and martensitic mechanical twinning were observed. Especially, in Ta13, we observe an undiscovered deformation mechanism, i.e., martensitic SA type II twinning to martensitic mechanical type I twinning transformation, which enables stress-induced α'', SA twins and nanomechanical twins to be sequentially activated. Detailed electron back-scatter diffraction (EBSD), transmission electron microscopy (TEM) analysis and infinitesimal deformation approach (IDA) calculations suggest that this dynamic martensitic twinning strengthening behavior stems from a re-selection of invariant plane for SA $<\bar{2}11>_{α''}$ type II twins during phase transformation, which energetically encourages the nucleation of a mechanical $\{351\}_{α''}$ type I twinning within SA "$\{351\}$"$<\bar{2}11>_{α''}$ type II twinned martensite to accommodate plastic deformation after early TRIP effect peaked. This SA type II twinning to mechanical type I martensitic twinning transformation mechanism not only maximizes the effect of TRIP and TWIP on imparting ductility to the metastable BCC-HEAs but also maintains a consistently strong dynamic strengthening effect that effectively suppresses the early plastic instability that frequently observed in conventional BCC alloys.

2. Experimental

The nominal compositions of the alloys investigated in the current work are $(TiZrHf)_{85}Ta_{15}$ and $(TiZrHf)_{87}Ta_{13}$ (at.%). The ingots of these alloys were synthesized by arc melting the pure metals (purity above 99.9 wt.%) under a Ti-gettered high-purity argon atmosphere. Ingots were remelted at least five times for chemical homogeneity and subsequently cast into a water-cooled copper mold with internal dimensions of $6 \times 7 \times 30$ mm. Samples were further homogenized in vacuum-sealed quartz tubes at 1473 K for 2 hours and subsequently quenched in water by breaking the tube simultaneously. Finally, after cold rolling with a reduction in thickness of 75%, the samples were annealed in vacuum-sealed quartz tubes at 1123 K for 0.5 hour and subsequently water quenched. The shear modulus (G) of annealed Ta13 and Ta15 alloys were determined using ultrasonic method (OLYMPUS EPOCH 650). Shear modulus can be expressed as $G = \rho V_s^2$[44], where V_s is the ultrasonic shear wave velocity and ρ is the density of the material. The bulk density of the Ta13 and Ta15 alloys were determined by the Archimedes method using a balance (New Classic MF MS104S/01) with an accuracy of ±0.0001 g. The actual composition analysis of the alloys was analyzed using an inductively coupled plasma method (ICP-OES instrument) and the oxygen content was determined by an inert gas fusion-infrared absorption method (Leco ONH836 instrument). The nominal chemical compositions for Ta15 and Ta13 are determined as $Ti_{27.98}Zr_{28.13}Hf_{28.03}Ta_{14.98}O_{0.88}$ and $Ti_{28.85}Zr_{28.79}Hf_{28.64}Ta_{12.85}O_{0.87}$ (at.%), respectively. The flat dog-bone-shaped tensile samples were cut by electrical discharge machining from the annealed plates with a gauge length of $3 \times 12.5 \times 1$

1   mm. Before testing, the samples were polished using P2000 grit SiC grinding paper

2   to remove the possible oxidation layer at surface. The tensile tests were then

3   performed on a ZWICK Z050TH testing system coupled with a laser extensometer at

4   a nominal strain rate of 4×10^{-4} s^{-1} at ambient temperature. Tensile tests were

5   performed along the rolling direction and at least 3 samples were tested for each

6   alloy. Another four tests were performed to total strains of 3%, 6%, 9% and 20% for

7   microstructural analysis. These strain levels were selected according to different

8   work hardening stages. Phase identification was carried out by X-ray diffraction

9   (XRD) on Bruker D2 Phaser with Cu-Kα (λ = 1.5406 Å) radiation source. The XRD

10 patterns of 20% strained Ta13 and Ta15 samples were analyzed by the Rietveld

11 refinement method using the TOPAS X-ray diffraction post-processing software to

12 identify lattice parameters of different phases as shown in Table. 1. The diffraction

13 patterns (DPs) identification and IDA calculations in following sections are all

14 conducted by using these identified lattice parameters.

15 **Table. 1**

16 Lattice parameters of α'' (cmcm) and β (Im-3m) phase and α'' c-axis transformation strain

17 in 20% strained Ta13 and Ta15.

| Sample	Space group	Lattice parameter (Å)			Transformation strain on c-axis
Ta13	cmcm	a = 3.193	b = 5.252	c = 4.931	η_3=0.014
	Im-3m	a=3.442			
Ta15	cmcm	a = 3.217	b = 5.235	c = 4.912	η_3=0.007
	Im-3m	a=3.451			

1

The microstructure and phase constitution analyses were carried out by a FEI Inspect F50 field emission gun scanning electron microscope (FEG-SEM) fitted with an Oxford Instruments electron back scatter diffraction (EBSD) detector operating at 25 kV with a step size of 0.05-0.2 µm, depending on the sample grain and deformation feature size. EBSD specimens were cut from gauge section with one straight edge, followed by mechanically polishing down to 3 µm diamond suspension and then ion polished with a Gatan PECS II ion polishing system under a condition of 3 kV, 5° for 15 minutes to remove possible contamination and residual deformation in the surficial layer induced by mechanical polishing. The quantitative analysis of EBSD data was performed by HKL's CHANNEL5 EBSD post-processing software and more than 20 grains were included for average grain sizes and phase fractions analysis for each sample. Detailed microstructural characterizations were completed by transmission electron microscopy (TEM). Thin foils were prepared by twin-jet electropolishing (Struers TenuPol 5) with a solution of 5% perchloric acid, 35% 2-butoxyethanol and 60% methanol. The foils were then put into a Gatan Precision Ion Polishing system (PIPS II) for final cleaning by ion polishing at 0.3 kV for 20 s. For low magnification imaging and selected area diffraction patterns (SADPs) analysis, a FEI Tecnai T20 TEM with an accelerating voltage of 200 kV were used. High-resolution microstructural characterization was performed by a Titan 80/300 and JEOL R005 spherical-aberration corrected TEM with an accelerating voltage of 300 kV.

3. Results

3.1. Tensile properties

Fig. 1a shows the representative mechanical responses of Ta13 and Ta15. Both samples demonstrate a combination of high strength and large ductility. With a decrease of Ta content from 15 at.% to 13 at.%, the ultimate tensile strength (UTS) increases from 994 MPa to 1310 MPa, while the elongation to fracture rises from 20% to 25%, which are attributed to the higher work hardening capability ($d\sigma_T/d\varepsilon_P$) of Ta13 as shown in Fig. 1b. More importantly, the normalized work hardening rate ($d\sigma_T/d\varepsilon_P$)/G ($d\sigma_T/d\varepsilon_P$ is the work hardening rate, and G is the bulk shear modulus) of Ta13 reaches 0.34 and notably outperforms that of high-performance TWIP[45,46] and TRIP polycrystalline alloys[31,47–50] which are well-known for their good work hardening capability (inset of Fig. 1a). According to the Kocks–Mecking model, the maximum theoretical value of the normalized work hardening rate for BCC and FCC alloys with only dislocation hardening is estimated to be merely ~0.055[51,52], so it is pertinent to speculate that additional deformation mechanisms have been triggered to account for the exceptional work hardening capability. Work hardening rates and their exponent curves in Fig. 1b and c suggest that there are five distinct hardening stages in Ta15 and Ta13, indicating different strengthening mechanisms may occur in different deformation stages. The initial rapid drop of work hardening rates corresponding to stage I (ε_T = 0-1.5%) indicates the start of plastic deformation after yielding[30]. Upon straining to stage II (ε_T = 1.5-4%), the work hardening rate increases greatly for both Ta13 and Ta15 to maximum values of 12.5 GPa and 6.8 GPa at ~4% strain, respectively. Meanwhile, similar to TRIP Ti

1 alloys[25,26,28,47,49,53], double yielding behavior was observed in both stress-

2 strain curves, which is attributed to the activation of martensitic transformation during

3 stage II. With further straining to stage III (ε_T = 4-6%), the work hardening rates drop

4 to 6 GPa and 4.2 GPa for Ta13 and Ta15, respectively. In stage IV (ε_T = 6-12%), the

5 work hardening rate decreases gradually but still maintains at a high level of 2-5 GPa

6 for both alloys. A small hump is observed in the work hardening exponent curves of

7 both alloys in the strain range between 6% to 9% (Fig. 1c). As illustrated in

8 multicomponent complex alloys[54], the rebound of the work hardening exponent

9 generally indicates the activation of an additional strengthening mechanism that

10 enables the sustainability of the high work hardening rate. In stage V (ε_T = 12-25%),

11 the work hardening rate of Ta15 decreases gradually, leading to fracture at 20%

12 strain. By contrast, in Fig. 1c, the work hardening exponent n of Ta13 exhibits a

13 steady increase from 0.22 at 12% strain to 0.31 at 22% strain before the end of stage

14 V, suggesting an extra strengthening mechanism may occur at late strain levels.
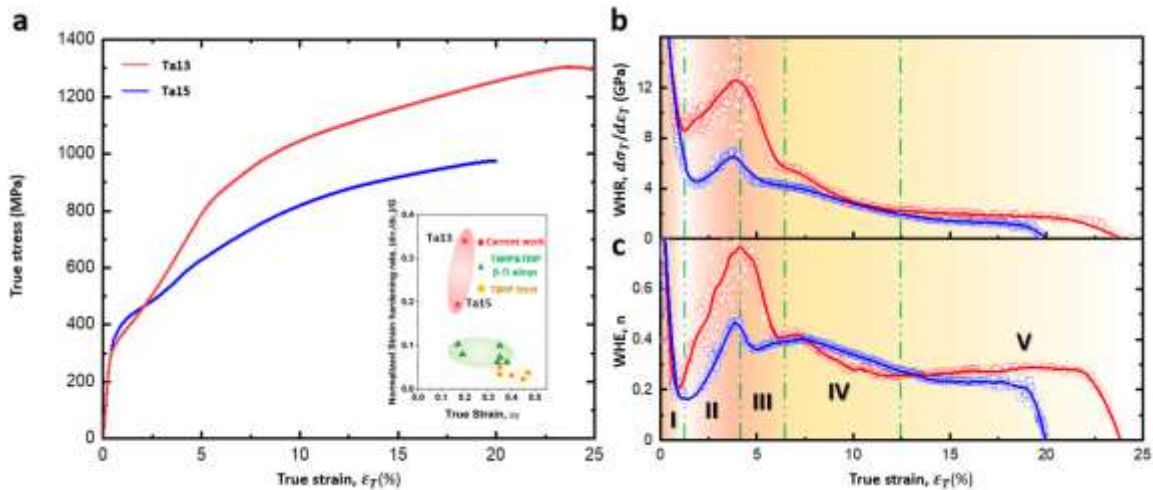
15

16 **Fig. 1.** Mechanical properties of (TiZrHf)$_{87}$Ta$_{13}$ and (TiZrHf)$_{85}$Ta$_{15}$. (a) the tensile true

17 stress–strain curves of Ta13 (red) and Ta15 (blue). Inset shows a comparison of the

1   normalized work hardening rate $((d\sigma_T/d\varepsilon_P)/G)$ as a function of elongation between the

2   present alloys and other high-performance Ti alloys[31,47–50] and TWIP steels[45,46].

3   (b) work hardening rate curves and (c) work hardening exponent curves of Ta13 (red) and

4   Ta15 (blue) as a function of true strain.   Five deformation stages are identified and

5   characterized as stage I-V.

6   *3.2 Microstructural characterization*

7   *3.2.1 XRD and EBSD analysis*

8   To describe the microstructural evolution and underlying deformation

9   mechanisms activated within different deformation stages, Fig. 2 shows XRD (Ta13)

10   and EBSD (Ta13 and Ta15) results obtained for the deformed samples at 0, 3, 6 and

11   9% strain. Only β phase was indexed in the annealed state for both Ta13 and Ta15

12   before deformation (Fig. 2a). When the strain increases to ε_T = 3%, a large amount

13   of α'' martensite plates with an average width of 1.27 μm and 1.19 μm are observed

14   in the β grains of Ta13 and Ta15, respectively (Fig. 2b and Table. 2). The volume

15   fractions of the martensite reach 11.2% and 8.7% for Ta13 and Ta15, respectively.

16   With further straining to ε_T = 6%, microstructural analysis shows that the primary α''

17   plates coarsen to 3 μm and 2.6 μm while the α'' volume fractions increase to 31%

18   and 24% for Ta13 and Ta15, respectively (Fig. 2c and Table. 2). At this strain, the

19   increased α'' fraction encourages the martensites to arrange themselves into a more

20   complex structure and results in a grain refinement effect in primary martensites,

21   leading to an average width of 0.67 μm and 0.97 μm for Ta13 and Ta15, respectively.

22   A further rise in the volume fractions of α'' to 43% and 34% in Ta13 and Ta15 at 9%

23   strain is observed (Fig. 2d and Table. 2), respectively, and at this stage, the average

24   α'' martensite sizes for Ta13 and Ta15 come to 0.33 μm and 0.67 μm. These

1   observations of substantial α'' martensite plates in β grain and complex

2   substructures within primary α'' martensites as observed in Fig. 2d validate that the

3   desired instability of the β phase motivates the formation of stress-induced α''

4   martensite and specific martensitic deformation products (i.e., SA and mechanical

5   twins) at different strain levels which keep splitting β grain and primary martensites.
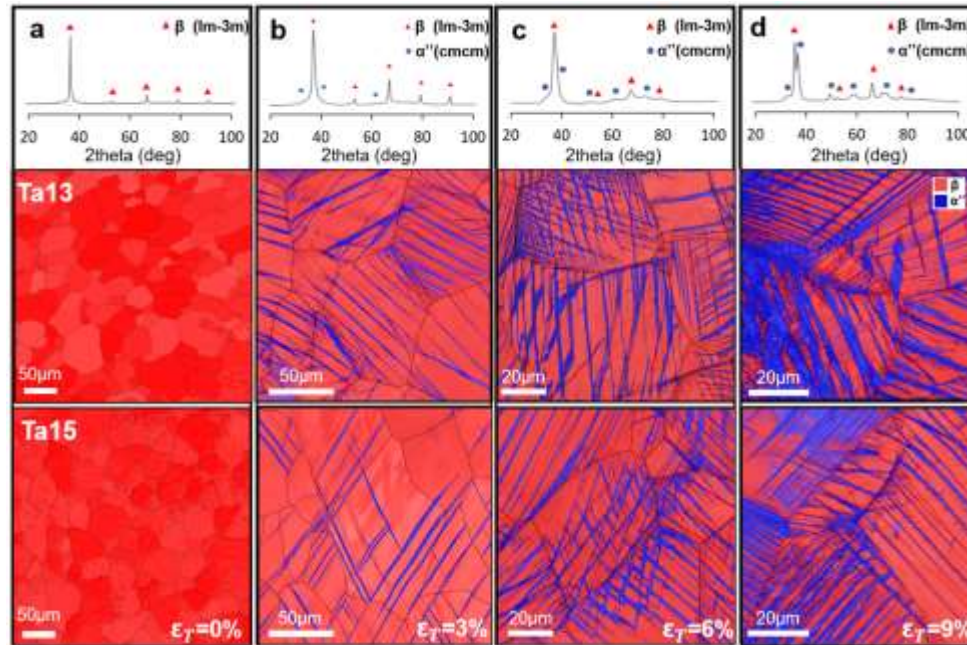
6

7   **Fig. 2.** Microstructural evolution of $(TiZrHf)_{87}Ta_{13}$ and $(TiZrHf)_{85}Ta_{15}$ with increase of

8   strain. XRD patterns of Ta13 and EBSD phase maps of Ta13 and Ta15 subjected to

9   (a) 0, (b) 3, (c) 6 and (d) 9% true strain.

10   **Table. 2**

11   Volume fraction and average thickness of α'' measured at different strain levels.

Strain levels (%)	Volume fraction of α'' (%)		Average thickness of α'' (μm)	
	Ta15	Ta13	Ta15	Ta13
3	11.2	8.7	1.27	1.19
6	31	24	0.67	0.97
9	43	34	0.33	0.67

1

In order to unravel the underlying mechanism for the multi-stage work hardening behavior and improved mechanical properties of Ta13, in Fig. 3, we derived the representative misorientation profiles of potential twinning related martensites (Table. 3) from EBSD data of Ta13 samples strained to 3% and 6% to identify the involved α'' martensitic twinning systems in the early deformation stages. The orientation relationship (OR) was investigated in detail by constructing stereographic projections from acquired crystallographic orientations of different twinning related martensites where directions of three-axis and the poles of interest martensites are marked for each constructed stereographic projections to ensure consistency, accuracy and readability. The misorientation axis/angle pair of 86.7°-$<011>_{\alpha''}$[55] is first identified in 3% strained Ta13 (Fig. 3a), which corresponds to a $\{111\}_{\alpha''}$ type I twinning system. In addition, a $<\bar{2}11>_{\alpha''}$ type II twinning system is observed with misorientation axis/angle pair of 96.4°-$<011>_{\alpha''}$. It is known that there are six crystallographically equivalent variants of α'' martensite in the β parent phase, in which the lattice correspondences between them are listed as $<100>_{\alpha''}//<100>_{\beta}$, $<010>_{\alpha''}//<011>_{\beta}$, $<001>_{\alpha''}//<01\bar{1}>_{\beta}$[41]. Both of $\{111\}_{\alpha''}$ type I and $<\bar{2}11>_{\alpha''}$ type II twinning systems are accepted as essential SA twinning systems to relate these martensitic variants for accommodating the α'' martensitic phase transformation induced volume misfit as analogous to that in metastable β-Ti alloys[38].
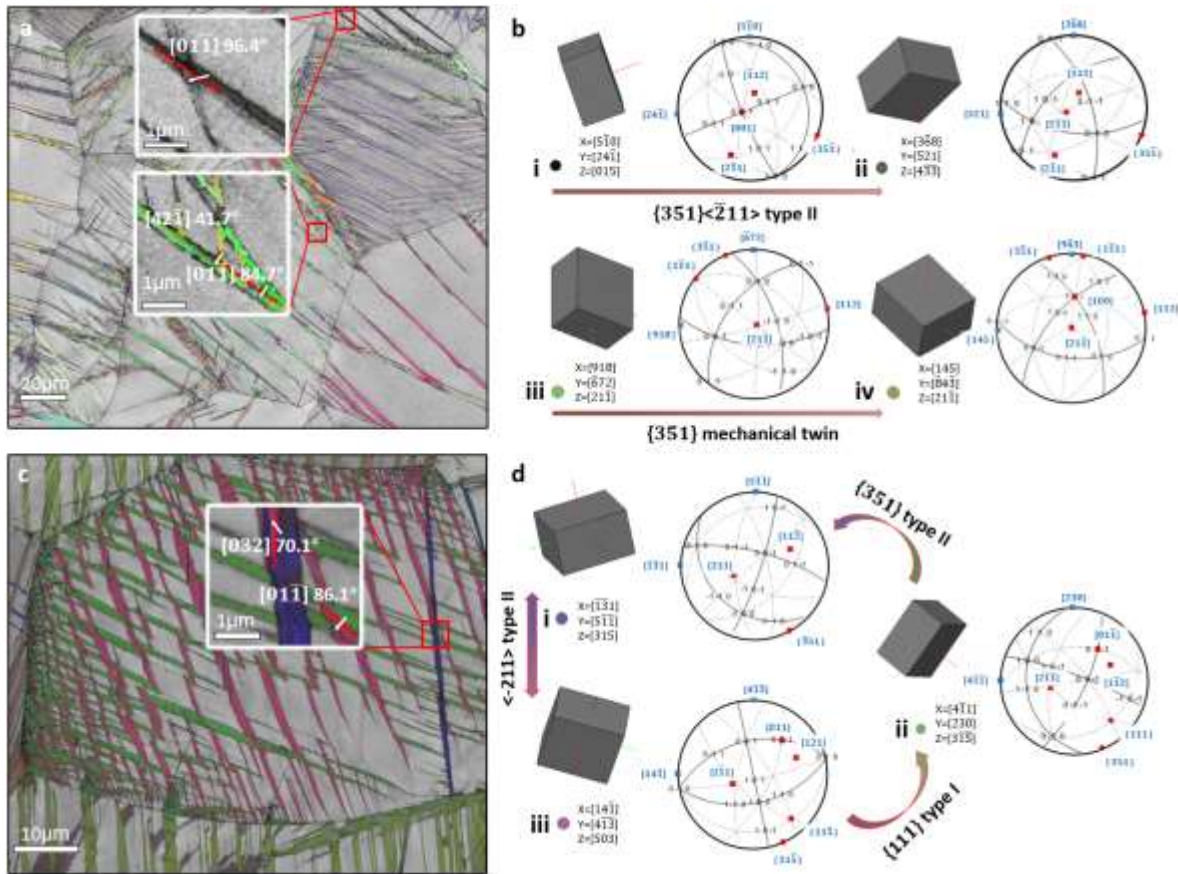
Fig. 3. Orientation relationship (OR) analysis with misorientation profile of α'' martensites acquired from EBSD of different strained Ta13. (a) Euler angle map of α'' phase superimposed on image quality (IQ) map of 3% strained Ta13. The insets are α'' features used for OR analysis. (b) Stereographic projections of white arrow highlighted martensites (i-ii: top boxed area in (a); iii-iv: bottom boxed area in (a)). (c) Euler angle map of α'' phase superimposed on IQ map of 6% strained Ta13. The inset is α'' features used for OR analysis. (d) Stereographic projections of white arrow highlighted martensites from the boxed area in (c). All crystallographic orientation data of highlighted martensites are marked with corresponding Euler angle colour, and stereographic projection figures are constructed with directions of three-axis and key poles of interest.

Table. 3

Misorientation profile of observed martensitic twins.

Misorientation angle	Misorientation axis	Twinning system
86°	$<011>_{\alpha''}$	$\{111\}_{\alpha''}$ type I twinning
96.4°/70°	$<011>_{\alpha''}/<032>_{\alpha''}$	$<\bar{2}11>_{\alpha''}$ type II twinning
47.1°	$<42\bar{1}>_{\alpha'''}$	$\{351\}_{\alpha''}$ type I twinning

1

2   Stereographic projections of the $<\bar{2}11>_{\alpha''}$ type II twinning related V-shaped

3 martensites in Fig. 3b(i) and b(ii), exhibit a common $(35\bar{1})_{\alpha''}$ pole, $[\bar{1}12]_{\alpha''}$ direction

4 and $[2\bar{1}1]_{\alpha''}$ direction, suggesting a coherent $(35\bar{1})_{\alpha''}$ twinning plane between the V-

5 shaped martensites. Therefore, according to the acquired crystallographic

6 orientations data of highlighted martensites in Fig. 3a(i, ii), a 180° rotation of the

7 martensite in Fig. 3a(i) along the $[2\bar{1}1]_{\alpha''}$ direction of the $(351)_{\alpha''}$ plane will result in

8 the martensite as orientated in Fig. 3a(ii), thereby demonstrating a $<\bar{2}11>_{\alpha''}$ type II

9 twinning relationship between them. By following conventional notations of denoting

10 rational or near rational indices with quotation marks in type II twins[53], this $<\bar{2}11>_{\alpha''}$

11 type II twinning system with an integral $\{351\}_{\alpha''}$ twinning plane is preliminarily

12 identified and designated as "$\{351\}$"$<\bar{2}11>_{\alpha''}$ type II twinning in present study, whilst

13 detailed characterizations of this twinning system, especially the "$\{351\}$"$_{\alpha''}$ twinning

14 plane, were conducted by TEM and HRTEM in following section. Meanwhile, at the

15 tips of some thin α'' plates in Fig. 3a, a third martensitic twinning system is captured

16 with a misorientation axis/angle pair of 47.1°-$<42\bar{1}>_{\alpha''}$, as shown in Fig. 3b(iii) and

17 b(iv). As illustrated in stereographic projections, the $(3\bar{5}1)_{\alpha''}$ poles in Fig. 3b(iii) and

18 3b(iv) are very close, with a misfit of 2.7 degrees, which can be accepted as a nearly

19 common pole between martensites[53]. Therefore, the highlighted martensites share

1   a nearly coherent $(3\bar{5}1)_{\alpha''}$ plane, while the $(3\bar{5}1)_{\alpha''}$ pole, the $[\bar{1}12]_{\alpha''}$ and $[2\bar{1}1]_{\alpha''}$

2   directions are nearly common. This observation suggests that this twinning structure

3   also utilizes the $\{351\}_{\alpha''}$ as the twinning plane but exhibits different symmetry

4   operation with the "$\{351\}$"$<\bar{2}11>_{\alpha''}$ type II twinning. After comparing the

5   misorientation profile of martensites shown in Fig. 3b(iii) and 3b(iv), a mirror

6   symmetry can be established across the $(3\bar{5}1)_{\alpha''}$ pole which is distinct to the "$\{351\}$"

7     $<\bar{2}11>_{\alpha''}$ type II twinning (180° rotation along the $<\bar{2}11>_{\alpha''}$ direction against the $\{351\}_{\alpha''}$

8   pole). Thereafter, the OR between them is preliminarily identified as a $\{351\}_{\alpha''}$

9   twinning which also utilizes the $\{351\}_{\alpha''}$ as the twinning plane but exhibits different

10   symmetry operation with the "$\{351\}$"$<\bar{2}11>_{\alpha''}$ type II twinning. The existence of a

11     $\{351\}<1\bar{1}2>_{t}$ compound twinning system has also been predicted by Tobe et al.[57]

12   by considering lattice instability in addition to the theory of the crystallography of

13   deformation twinning[62] in a base centered tetragonal (BCT) structure that close to

14   the α" structure, whilst similar prediction of a $\{351\}$ type I mechanical twinning system

15   has also been proposed by Crocker[58] in orthorhombic α-uranium. Accordingly,

16   current observation agrees with their predictions and indicates that the observed

17     $\{351\}_{\alpha''}$ twinning is a mechanical $\{351\}_{\alpha''}$ type I twinning mode whose twinning

18   direction may be approximated to $<1\bar{1}2>_{\alpha''}$ and indices are probably irrational (more

19   related analysis in identifying its mechanical twinning nature will be performed in the

20   following contents). Therefore, to clarify differences in twinning operations between

21   the two $\{351\}_{\alpha''}$ twinning, and by following conventional notations of denoting near

22   rational indices with quotation marks, this twinning system is denoted as

23     $\{351\}$"$<1\bar{1}2>$" type I twinning in present work.

1   In the 6% strained sample (Fig. 3c), related by same α'' matrix (Fig. 3d(ii)), the

2 "{351}"<$\bar{2}11$>$_{\alpha''}$ type II twinned martensite (Fig. 3d(i)) is observed exhibiting

3 <032>$_{\alpha''}$~70° with respect to the {111}$_{\alpha''}$ type I twinned martensite (Fig. 3d(iii)). By

4 calculating the lattice correspondence between α'' matrix and twinned variant of

5 different twinning modes (Table. 4), twinning relationship between α'' martensites

6 can be preliminarily identified after comparing their observed lattice correspondence

7 with calculated ones[59,60]. It is observed that [503]$_{\alpha''}$ (Z direction) of the martensite

8 in Fig. 3d(iii) is parallel to [315]$_{\alpha''}$ (Z direction) of the martensite in Fig. 3d(i), which

9 corresponds to the "{351}"<$\bar{2}11$>$_{\alpha''}$ type II twinning relationship. Thus, the

10 misorientation axis/angle pair <032>$_{\alpha''}$~70° is regarded as a special case of <$\bar{2}11$>$_{\alpha''}$

11 type II twinning and has been added to Table. 4.

12 **Table. 4**

13 Lattice correspondence between α'' matrix and twinned variant for different crystallographic

14 twinning operations. (The miller indices are rounded into integer for convenience).

Twinning operation	Main lattice correspondence between α'' matrix and twinned variant					
α'' Matrix	<100>	<001>	<10$\bar{1}$>	<1$\bar{1}$2>	<2$\bar{1}$1>	<503>
"{351}"<$\bar{2}$11>$_{\alpha''}$ type II twinning	<011>	<2$\bar{1}$1>	<1$\bar{1}$0>	<1$\bar{1}$2>	<001>	<315>
{351}$_{\alpha''}$ type I twinning	<2$\bar{7}\bar{1}$>	<$\bar{1}\bar{1}$4>	<1$\bar{1}\bar{2}$>	<1$\bar{1}$2>	<8$\bar{8}$5>	<021>

15   Further straining to 9% results in a significant increase of the martensites and

16 twinning boundary density in Ta13. In Fig. 4, the three identified martensitic twinning

17 boundaries corresponding to {351}$_{\alpha''}$ type I twinning, {111}$_{\alpha''}$ type I twinning and

18 "{351}"<$\bar{2}$11>$_{\alpha''}$ type II twinning are marked in the image quality maps of 9% strained

Ta13 (Fig. 4a). In contrast to the morphology of the martensitic SA twinning observed at 3% and 6% strained samples that mostly exhibit a V shaped structure, the SA twinned martensite nucleated within the primary martensite while the mechanical twinning initiated from the lateral boundaries of the primary martensite plates (Fig. 4a). Kernel average misorientation (KAM) analysis was further carried out to present the local misorientation level of the α'' phase at 9% strain (Fig. 4b). As the geometrically necessary dislocation (GND) density of deformed microstructures could be evaluated from the KAM value[61], the high misorientation value observed at the intersection regions of martensitic SA and mechanical twinning boundaries in α'' phase suggests that SA twins share similar effectiveness with mechanical twins in preventing the dislocation movements[62,63]. After 20% strain, microstructural characterization results of Ta13 in Fig. 4c show that martensites have ubiquitously embedded in the β grain and interacted with each other, forming intricate networks which dramatically refined the martensite plates.
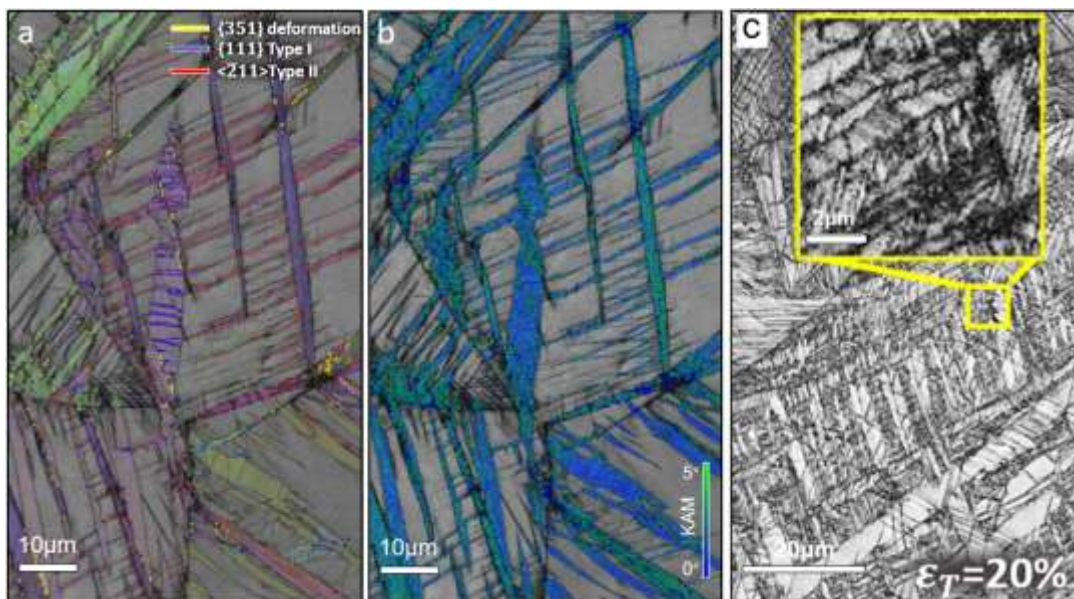
Fig. 4. Deformation microstructure of Ta13 at different strains. (a) Martensitic twins at 9% true strain in Ta13 revealed by EBSD. Image quality and Euler angle map of α'' phase with yellow, blue and red lines representing twinning boundaries of $\{351\}_{α''}$ type I twinning, $\{111\}_{α''}$ type I twinning and "$\{351\}$"$<\bar{2}11>_{α''}$ type II twinning, respectively. (b) KAM map of the α'' phase. (c) Microstructural image of Ti13 at 20% strain.

3.2.2 TEM identification of martensitic twins

Owing to the limits of the EBSD technique (i.e., relatively low resolution and pseudo-symmetry[64]) in identifying the martensitic twinning system and nano-scale deformation products (i.e., nano-twinning and stacking faults), TEM observations were conducted. A featured region with various deformation products in 6% strained Ta13 is captured in Fig. 5a. Fig. 5b shows corresponding selected area diffraction patterns (SADPs) acquired on the interface of the deformation bands. The DPs of the two involved martensites exhibit mirror symmetry against the $(351)_{α''}$ plane which indicates the observed feature is a $(351)_{α''}$ twinning (the exact twinning identification of this twinning will be conducted in following contents with SADPs acquired from different diffraction conditions in Fig. 6). Needle-like straight laths with ~40nm width are observed within the primary twinned variant in the dark-field images (DFIs) taken from $(\bar{1}11)_{α''M}$ and $(\bar{1}11)_{α''T}$ reflections (Fig. 5c(i) and Fig. 5c(ii)), while dense serrated laths observed across the α'' plates are identified as anti-phase boundary (APB) like stacking faults from the DFIs taken with $g^* = 110$ (Fig. 5c(iii) and Fig. 5c(iv)). These wavy APB domains may further serve as nuclei for new martensites to accommodate specific shear within the primary martensite[65,66].
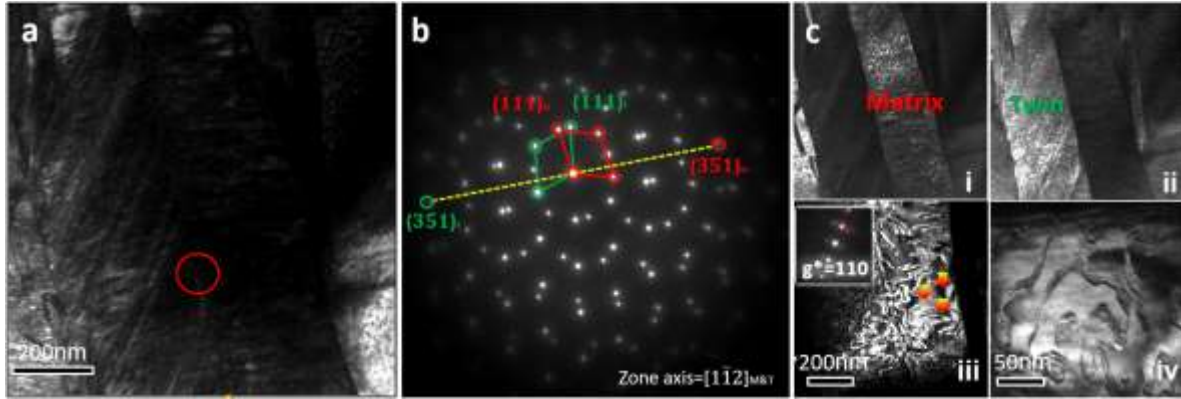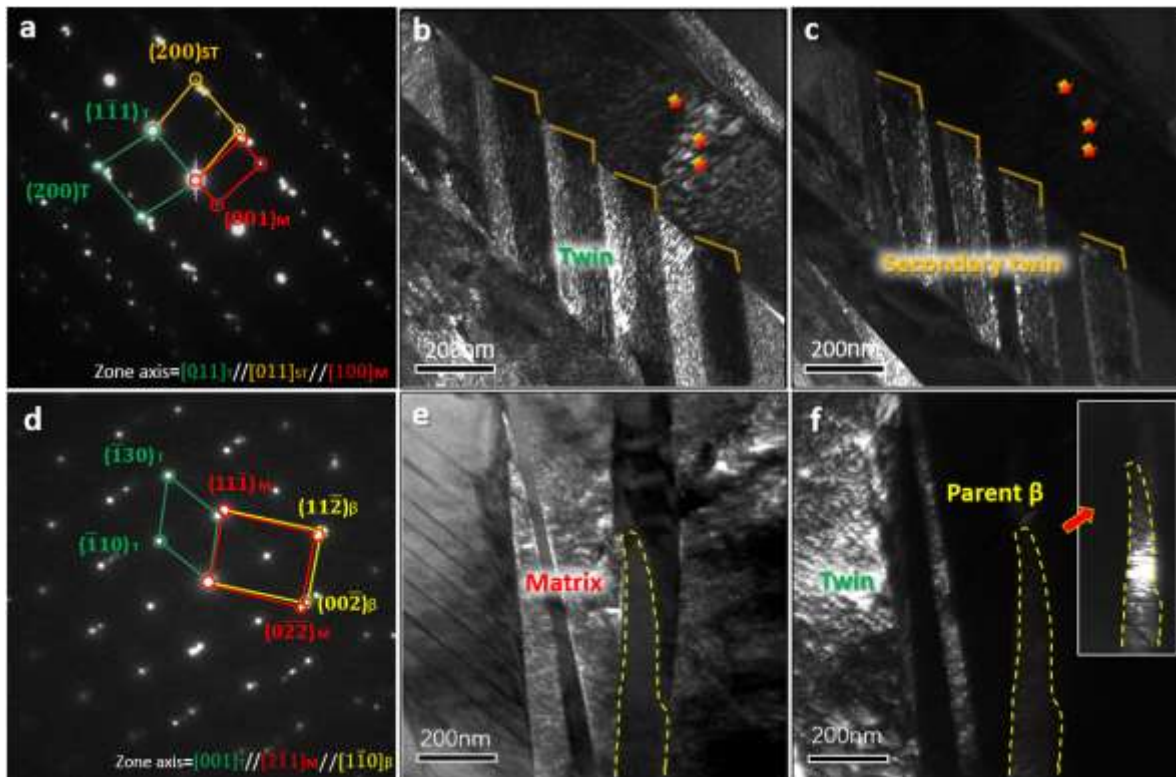
Fig. 5. TEM images of deformation bands in the deformed Ta13 specimen at 6% strain. (a) BFI of the deformation band. (b) SADPs taken from the twinning boundary (marked by red circle in (a)) taken along the $[1\bar{1}2]_{\alpha''}$ zone axis. The α'' matrix (M) and twinned α'' variant (T) diffraction spots are marked with red and green open circles, respectively. (c) DFIs of the twinning, and APB-like stacking faults with $g^* = 110$ in $[\bar{1}10]_{\alpha''}$ zone axis.

Via re-tilting the featured area of Fig. 5a, in Fig. 6, the lattice correspondence between α'' matrix and α'' twinned variant is clarified as $[100]_{\alpha''M}//[011]_{\alpha''T}$ (Fig. 6a) and $[2\bar{1}1]_{\alpha''M}//[001]_{\alpha''T}$ (Fig. 6d) which matched well with the calculated lattice correspondence of "{351}"$<\bar{2}11>_{\alpha''}$ type II twinning as listed in Table. 3. Therefore, the observed twinning in Fig. 5 is confirmed as SA "{351}"$<\bar{2}11>_{\alpha''}$ type II twinning. From the SADPs in Fig. 6a, the OR between the secondary α'' twinned laths and primary type II twinned α'' variant (Fig. 6b and c) is clarified as {111}$_{\alpha''}$ type I twinning, and the lattice correspondence between α'' twinning and parent β grain is identified to be $[2\bar{1}1]_{\alpha''M}//[001]_{\alpha''T}//[1\bar{1}0]_{\beta}$ by referring to SADPs in Fig. 6d. This specific lattice correspondence agrees with the lattice correspondence of the crystallographically equivalent variants of α'' martensite in the β parent phase which confirms that the SA "{351}"$<\bar{2}11>_{\alpha''}$ type II twinning shows low misfit with the parent β grain. This observation verifies the nature of SA twinning that can embed into a β grain in a

20

1 coherent manner where the corresponding β grain orientation will not be

2 changed[43].

3

4 **Fig. 6.** TEM images of the re-tilted deformation bands in Fig. 5a, (a) corresponding SADPs

5 taken along the $[100]_{\alpha''M}$//$[011]_{\alpha''T}$ zone axis. The α'' matrix (M), twinning (T) and secondary

6 twinning (ST) diffraction spots are marked with red, green and orange open circles,

7 respectively. (b, c) DFIs of the primary twinning and secondary twinning. (d) SADPs taken

8 along the $[2\bar{1}1]_{\alpha''M}$//$[001]_{\alpha''T}$ zone axis. The diffraction spots corresponding to α'' matrix, α''

9 twinning and parent β grain are marked with red, green and yellow open circles, respectively.

10 (e, f) DFIs of the α'' matrix and twinned variant, inset is DFI of the retained parent β grain.

11 It has been generally accepted that the twinning plane of type II twinning in α''

12 martensite is irrational[41], which is in contrast with our observation in Fig. 5. We

13 further conducted high-resolution transmission electron microscopy (HRTEM) to

14 investigate the development of the rational twinning plane in the newly observed

1   "{351}"<$\bar{2}$11>$_{α''}$ type II twinning. In Fig. 7a, HRTEM image of the twinning boundary

2   highlights that the "{351}"<$\bar{2}$11>$_{α''}$ type II twinning exhibits an exact mirror symmetry

3   against the (351)$_{α''}$ plane when viewed along the [1$\bar{1}$2]$_{α''}$ direction. A set of shuffled

4   atomic columns (orange) along the (110)$_{α''}$ planes in α'' martensite can be

5   distinguished from the origin columns (blue) in the magnified twinning boundary

6   image (Fig. 7b), due to the {1$\bar{1}$0}<110>$_β$ (lattice correspond to (001)<010>$_{α''}$)

7   instability (the origin of β to α'' transformation)[57,67]. Moreover, owing to the

8   twinning operation, the shuffled atomic columns are not only visible in the α'' matrix

9   but also can be found in the twinned α'' variant.
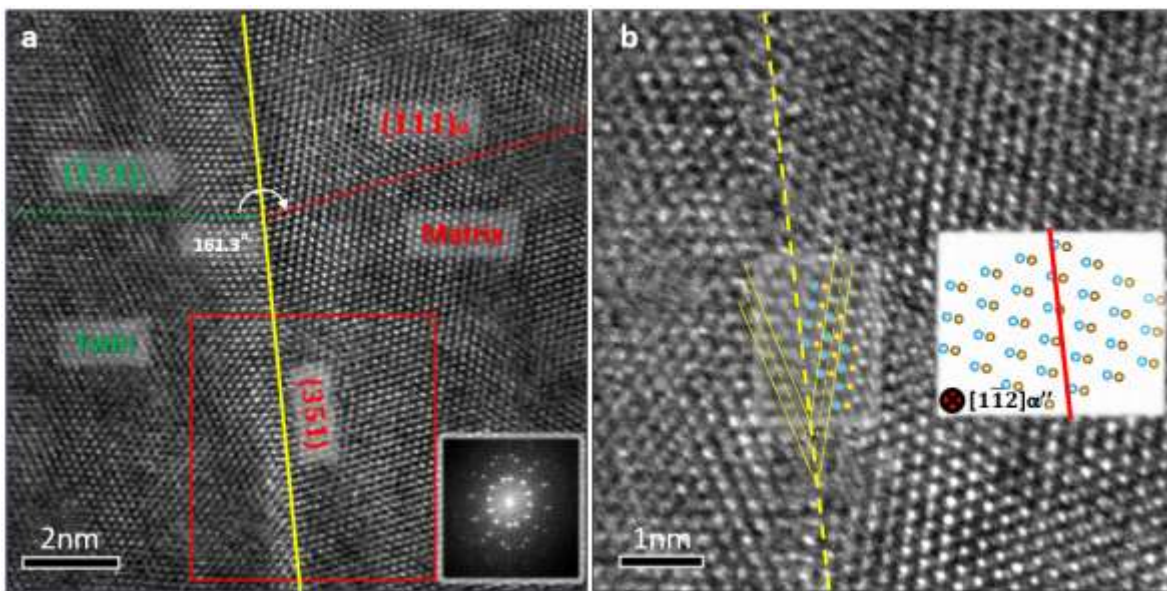
10

11   **Fig. 7.** Atomic-scale characterization of the "{351}"<$\bar{2}$11>$_{α''}$ type II twinning in deformed

12   Ta13 specimen at 6% strain. (a) HRTEM image of the {351}$_{α''}$ twinning boundary. Inset

13   shows the Fast Fourier transform (FFT) pattern of the twinning interface (red box marked

14   region). (b) Magnified HRTEM image of the twinning boundary (boxed region in a). Insets

15   are Wiener filtered image and schematic atomic configuration of the α'' matrix. The atomic

columns in the α'' matrix and columns shuffled with $(001)<010>_{\alpha''}$ displacement are highlighted by blue and orange dots, respectively.

   The α'' twinned variants adopt a more complex arrangement to accommodate the increased strain when the strain level reaches 9%. Fig. 8a displays a complex deformation microstructure consisting of various hierarchical nano-sized bands. The corresponding SADPs taken from the interface between the deformation bands along the $<\bar{1}12>_{\alpha''}$ zone axis are presented in Fig. 8b. In Fig. 8b, four α'' variants are identified and designated as V1-V4. SADPs of the same deformed feature in Fig. 8a taken from $<\bar{2}11>_{\alpha''}$ is provided in Fig. 8c for a better distinguishability when identifying the involved martensitic twins in later section. DFIs of V1-V4 are shown in Fig. 8d-f, showing the distribution and size of the four α'' variants.
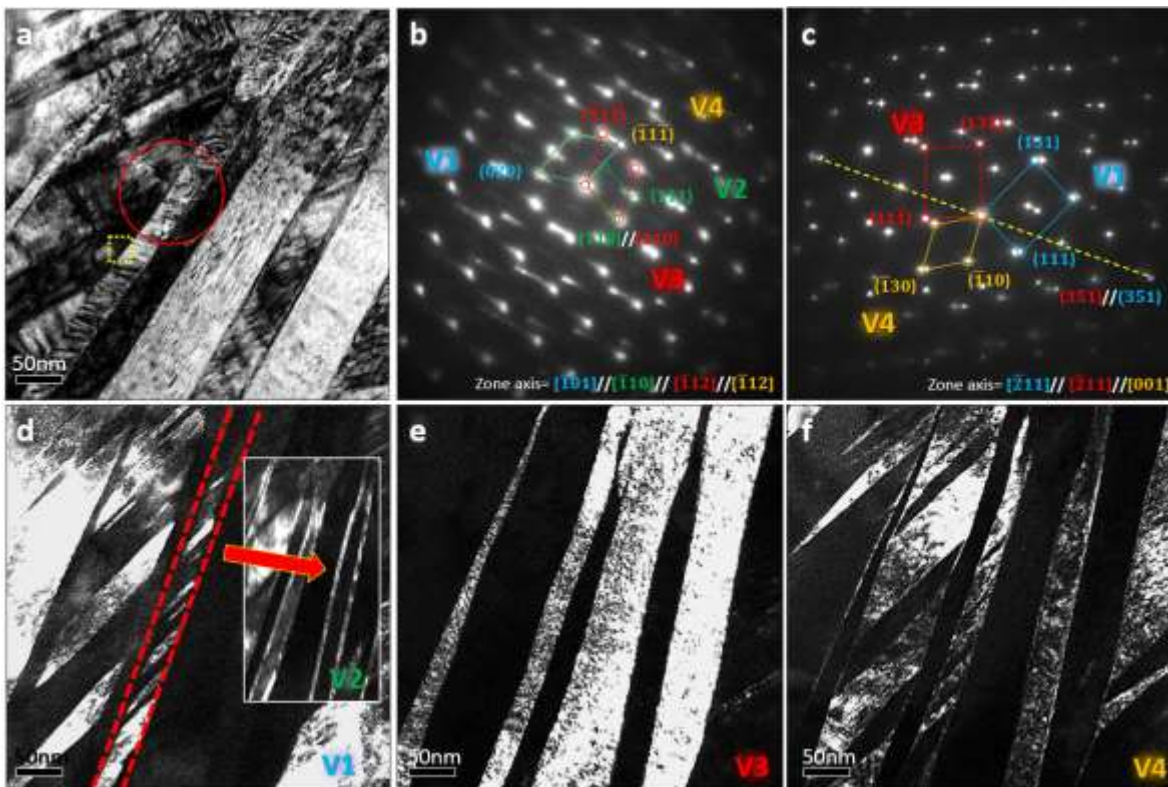
Fig. 8. TEM images of complex deformation bands in 9% strained Ta13. (a) BFI of the complex deformation bands. (b) and (c) are SADPs taken next to the twinning boundary (red circled area in (a)), along the $[\bar{1}01]_{\alpha''V1}$//$[\bar{1}10]_{\alpha''V2}$//$[\bar{1}12]_{\alpha''V3\&V4}$ and $[\bar{2}11]_{\alpha''V1-3}$//$[001]_{\alpha''V4}$ zone axes, respectively. DPs of V1-V4 are highlighted with blue, green, red and orange open circles, respectively. (d-f) DFIs correspond to V1-V4 α'' variants, respectively (taken from the spots of V1-V4 in (b)).

We then analyzed the OR between the four α'' variants. From the SADPs in Fig. 8b, the lattice correspondence between V1-V4 is identified as $[\bar{1}01]_{\alpha''V1}$//$[\bar{1}10]_{\alpha''V2}$//$[\bar{1}12]_{\alpha''V3\&V4}$. The crystallographic orientational mirror symmetry across the $(35\bar{1})_{\alpha''V3\&V4}$ plane (spots marked with white open circles in Fig. 8b) is established for V3 and V4, thereby exhibiting the "$(35\bar{1})$"$[2\bar{1}1]_{\alpha''}$ type II twinning relationship which is consistent with the observation in Fig. 5b. As the reflections of V2 in Fig. 8b is too weak to index, for better discernibility, in Fig. 9a, a FFT image is performed on the yellow boxed area in Fig. 8a where the martensite bands corresponding to V1, V2 and V3 are included. Through simulating the reflections of the involved V1-V3 martensites (Fig. 9b-d), stereographic projections are constructed from the acquired crystallographic orientation data in Fig. 9e-g with key poles of interest. Between V1, V2 and V3, a common $(351)_{\alpha''}$ pole and common $[\bar{2}11]_{\alpha''}$ and $[1\bar{1}2]_{\alpha''}$ directions are observed in Fig. 9e-g, which indicates a perfect lattice correspondence of the $(351)_{\alpha''}$ plane among V1-V3. Taken together with the OR identified in Fig. 8b where $[\bar{1}01]_{\alpha''V1}$//$[\bar{1}10]_{\alpha''V2}$, by referring to Table. 4, V2 is preliminarily identified as a "(351)"$[\bar{2}11]_{\alpha''}$ type II twinned variant of V1. In order to clarify the OR between V1 and V3, the SADPs imaged from $[\bar{2}11]_{\alpha''V1}$ zone axis of

1   the same area in Fig. 8c is taken into consideration for OR identification. The DPs of

2   V1 and V3 exhibit mirror symmetry with respect to the $(351)_{\alpha''V1,\ V3}$ reflection as

3   highlighted in Fig. 8c. Together with the lattice correspondence between V1 and V3

4   captured in Fig. 8b as additional reference ($[\bar{1}01]_{\alpha''V1}//[\bar{1}12]_{\alpha''V3}$), by referring to Table.

5   4, the twinning relationship between V1 and V3 is confirmed as $\{351\}_{\alpha''}$ type I

6   twinning. Taken together, the OR between V1-V4 is identified as: V1 is "(351)"$[\bar{2}11]_{\alpha''}$

7   type II twinning related to V2 and $(351)_{\alpha''}$ type I twinning related to V3, while V3 and

8   V4 are related by "$(35\bar{1})$"$[2\bar{1}1]_{\alpha''}$ type II twinning.

9
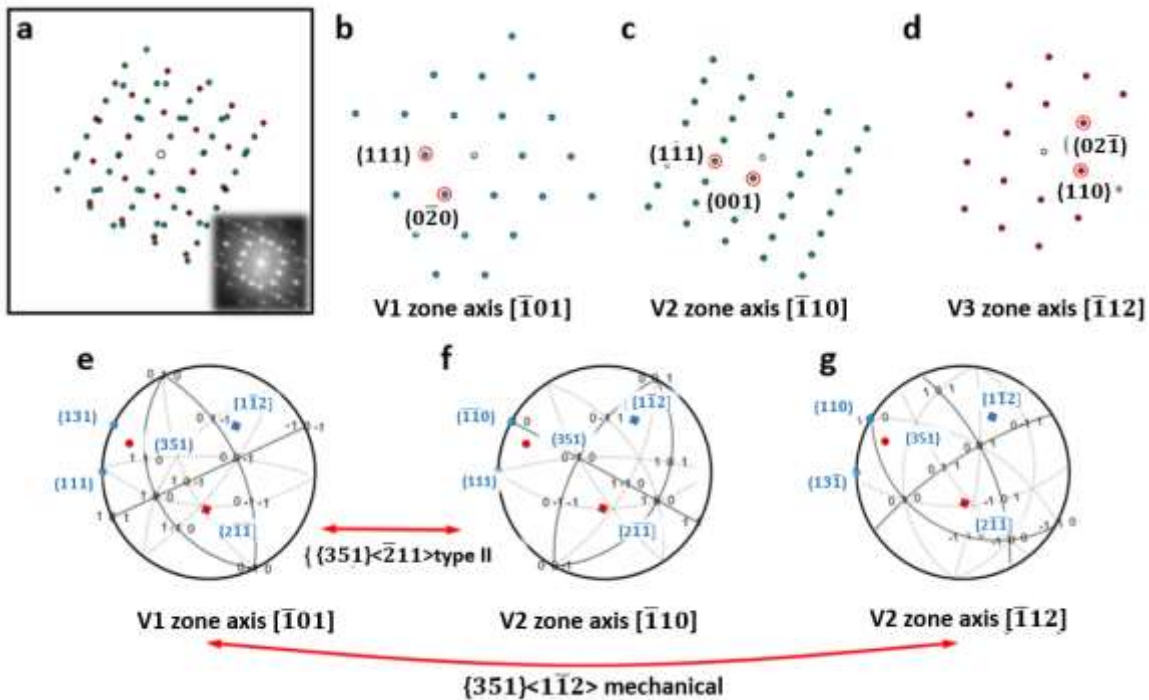
11   **Fig. 9.** Crystallographic orientations of the α'' phase represented as stereographic

12   projections used to determine the ORs between α'' matrix and twinned variants. (a) FFT and

13   simulated SADPs of the yellow dash boxed area in Fig. 8a imaged along the

14   $[\bar{1}01]_{\alpha''V1}//[\bar{1}10]_{\alpha''V2}//[\bar{1}12]_{\alpha''V3}$ zone axis. (b-d) Simulated DPs of $[\bar{1}01]_{\alpha''V1}$, $[\bar{1}10]_{\alpha''V2}$ and

1 $[\bar{1}12]_{\alpha"V3}$. (e-g) Stereographic projection figures of V1-V3 are constructed respectively from

2 the orientation data acquired from FFT in (a).

3   To understand the origin of the complex nanoscale interfacial substructure, the

4 feature in Fig. 8a was further analyzed using HRTEM to characterize the underlying

5 twinning evolution mechanism in Fig. 10. Imaging along the $[\bar{1}12]_{\alpha"V1}$ zone axis, V2

6 with a width of ~ 2nm is observed between V1 and V3 in Fig. 10a. On the basis of

7 the established OR between V1-V3 as shown in Fig. 9e-g, the $(351)_{\alpha"}$ plane is

8 confirmed as a coherent plane between V1, V2 and V3 which indicates that two

9 edge-on $(351)_{\alpha"}$ planes of V2 in Fig. 10a are both serving as twinning plane for V1-

10 V2 and V3-V2, respectively. When the same area is re-tilted to the $[-211]_{\alpha"V1}$ direction

11 that is parallel to the $(351)_{\alpha"}$ twinning plane, the lattices of V1 and V3 become

12 symmetrical with respect to the $(351)_{\alpha"}$ twinning plane. However, it needs to be noted

13 that the lattices of V2 become hard to distinguish in Fig. 10b which is attributed to

14 the viewing direction and special lattices arrangement of the "(351)"$[\bar{2}11]_{\alpha"}$ type II

15 twinning (OR between V1 and V2) as discussed in following contents.

16   To illustrate the underlying microstructural evolution process of this planar

17 feature, a schematic representation is presented in Fig. 10c. Owing to the

18 characteristic type II twinning operation, the "(351)"$[\bar{2}11]_{\alpha"}$ type II twinning (Fig.

19 10c(i)) only exhibits mirror symmetry against the $(351)_{\alpha"}$ twinning plane when viewed

20 along the $[1\bar{1}2]_{\alpha"}$ zone axis (nearly perpendicular to $[\bar{2}11]_{\alpha"}$). Moreover, when the

21 "(351)"$[\bar{2}11]_{\alpha"}$ type II twinning is viewed along the $[\bar{2}11]_{\alpha"}$ direction, the operation of

22 $<\bar{2}11>_{\alpha"}$ type II twinning rotates the α" matrix (V1) by 180 degrees along

23 "(351)"$[\bar{2}11]_{\alpha"}$, which indicates that the resulted type II twinned variant (V2) will

1   exhibit similar lattice arrangement as the α'' matrix as shown in Fig. 10c(ii). Therefore,

2   the boundary between "(351)"$[\bar{2}11]_{α''}$ type II twinning related V1 and V2 becomes

3   difficult to distinguish which results in the feature observed in Fig. 10b. According to

4   the reported mechanical twinning nucleation process in orthorhombic

5   α''[57,58,68,69], the biggest obstacle for the direct activation of $\{351\}_{α''}$ type I

6   mechanical twinning is the displacive atomic shuffle, which requires additional

7   atomic shuffle that greatly deviate from the twinning shear direction to move one-half

8   of the atoms to the appropriate twinned lattice sites after twinning shear[57].

9   However, as shown in Fig. 10c(ii) to Fig. 10c(iii), such additional atomic shuffle

10   becomes unnecessary when the nucleation of $\{351\}_{α''}$ type I mechanical twinning

11   initiates within the primary "$\{351\}$"$<\bar{2}11>_{α''}$ type II twinned variant which indicates

12   that just pure shear along the twinning shear direction (setting as $<1\bar{1}2>_{α''}$ for

13   simplification and better understanding) is required to nucleate the type I twinned

14   variant V3 along the $(351)_{α''}$ plane within the pre-existed type II twinned V2.
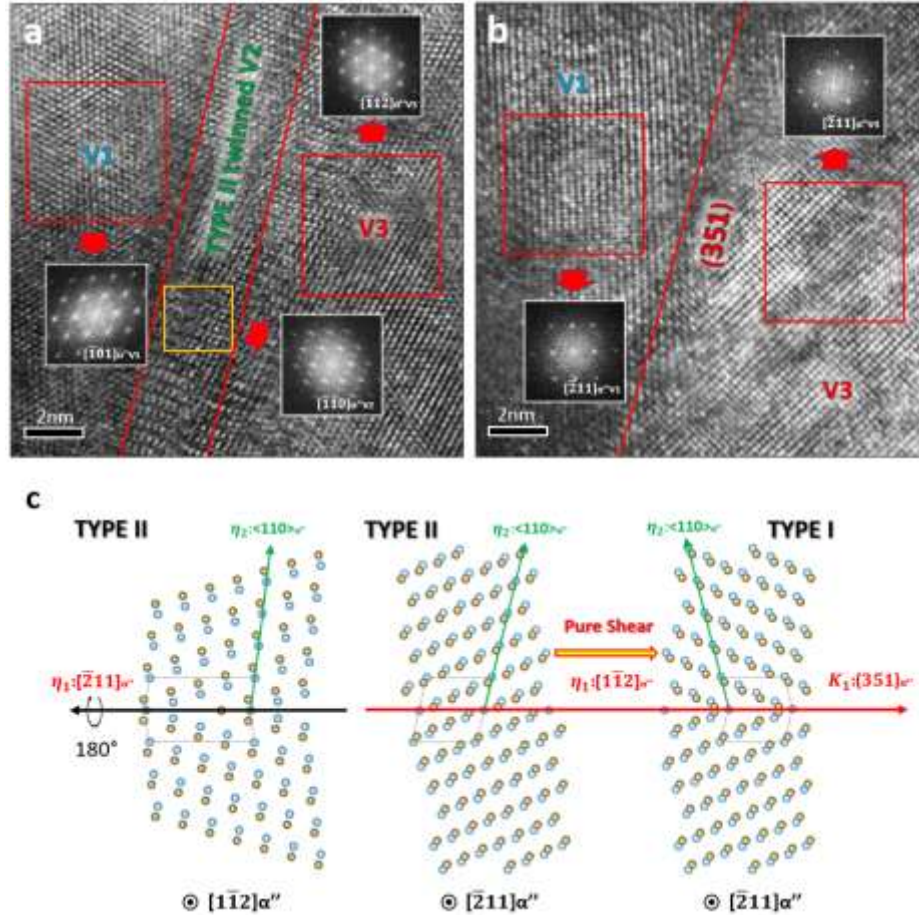
Fig. 10. Microstructural evolution of SA "{351}"<$\bar{2}$11>$_{\alpha''}$ type II twinning to mechanical {351}$_{\alpha''}$ type I twinning in 9% strained Ta13. (a) HRTEM image of the yellow boxed area in Fig. 8a. Insets are FFTs of red boxed regions. (b) HRTEM image of the same area in (a), acquired from [$\bar{2}$11]$_{\alpha''V1\&V3}$ direction. Insets are FFTs of red boxed regions. (c) Schematic illustration of atomic movements associated with the twinning evolution. Blue and orange dots indicate atoms at the α'' matrix and shuffled with (001)< 010>$_{\alpha''}$ (lattice correspond to {1$\bar{1}$0}<110>$_{\beta}$) displacement, respectively. Images from i-iii (left to right) are projections of "{351}"<$\bar{2}$11>$_{\alpha''}$ type II twinning along [1$\bar{1}$2]$_{\alpha''}$ and [$\bar{2}$11]$_{\alpha''}$ directions, {351}$_{\alpha''}$ type I twinning along [$\bar{2}$11]$_{\alpha''}$ direction, respectively.

A Schmid analysis was conducted to further illustrate the observed martensitic twinning transformation in Fig. 10. By using the lattice parameter of α'' in Ta13, the

exact twinning elements of the $\{351\}_{\alpha''}$ type I twinning are calculated by following the

Bilby-Crocker deformation twinning theory[70] as K1=$\{\,351\,\}_{\alpha''}$, η1="$< 11\bar{8} >$"$_{\alpha''}$,

K2="$\{001\}$"$_{\alpha''}$, η2=$<110>_{\alpha''}$, s=0.5407, where K1 is the twinning plane, η1 is the

twinning direction, K2 and η2 are their conjugate twinning elements and s is the

shear vector (The miller indices of twinning elements are rounded into integer for

convenience). Together, Schmid analysis of the $\{\,351\,\}$ type I twinning and

"$\{351\}$"$<\bar{2}11>_{\alpha''}$ type II twinning are conducted for the matrix martensite (V1) in Fig.

10 with the tensile direction measured as $[10\,8\,9]_{\alpha''}$ and listed in Table. 5. It is known

that a twinning mode is possible to be activated only with Schmid factor larger than

0.3[71]. By referring to Table. 5, the $(351)_{\alpha''}$ type I mechanical twinned variant (V3 in

Fig. 10) possesses the highest SF value among the calculated twinning modes which

explains its mechanical twinning nature and agrees well with our observation in Fig.

10. It needs to be noted that although the $(351)[\,\bar{2}11]_{\alpha''}$ type II twinned variant (V2 in

Fig. 10) possesses the second-largest SF, the prior activation of SA $(351)[\bar{2}11]_{\alpha''}$

type II twinning is attributed to the phase transformation process that generally

occurred before the plastic deformation of the martensite[43,72]. This explains the

priority of the SA $(351)[\,\bar{2}11]_{\alpha''}$ type II twinned variant (V2) over the mechanical $(351)_{\alpha''}$

type I twinned variant (V3) in V1. Current results indicate that the newly discovered

martensitic twinning transformation mechanism obeys the Schmid law where the

type II to type I twinning transformation will be activated once energetically preferred

loading is applied. Therefore, the microstructural evolution process can be confirmed

as: α'' matrix (V1)→"$\{351\}$"$<\bar{2}11>_{\alpha''}$ type II twinning (V2)→$\{351\}_{\alpha''}$ type I twinning (V3).

This specific activation sequence provides a novel type II to type I twinning

1 transformation mechanism which revealing the individual steps of martensitic

2 twinning transformation mechanism.

3 **Table. 5**

4 Schmid factor values of each twinning modes for "{351}"<$\bar{2}$11>$_{\alpha''}$ type II and {351}$_{\alpha''}$ type I

5 twinning systems (the values of activated modes are in bold).

K_1	η_1	SF
(351)	[$\bar{2}$11]	**0.3006**
($\bar{3}$51)	[211]	0.1974
(3$\bar{5}$1)	[$2\bar{1}$1]	0.0033
(35$\bar{1}$)	[$\bar{2}$1$\bar{1}$]	-0.1991
(351)	[$\bar{1}\bar{1}$8]	**0.4393**
($\bar{3}$51)	[1$\bar{1}$8]	0.1207
(3$\bar{5}$1)	[$\bar{1}$18]	-0.0073
(35$\bar{1}$)	[$\bar{1}\bar{1}$8]	-0.4925

6 We further analyzed the Ta13 deformed to 20% strain. In agreement with the

7 microstructure characterized in Fig. 4c, a complex network of the martensite bands

8 is observed and believed to be the predominant deformation products at this stage

9 (Fig. 11a). In Fig. 11b, SADPs taken from the twinning intersection area exhibit

10 reflections of four martensites, consisting of {111}$_{\alpha''}$ type I and {011}$_{\alpha''}$ compound

11 twins. DFIs in Fig. 11c-f highlight the distribution of the intersected twinning structure.

12 To elucidate the origin of this complex intersected twinning structure, OR analysis

13 was conducted on the four α'' variants involved in Fig. 11b. For convenience, the

14 four martensites were divided into M and V group by {111}$_{\alpha''}$ type I and {011}$_{\alpha''}$

15 compound twinning relationship, respectively. The overall lattice correspondences

16 of M and V group martensites can be acquired by constructing stereographic

1 projection figures from the acquired crystallographic orientation data of M1 and V2

2 with key poles of interest in Fig. 11g and h, respectively. With well-matched lattice

3 correspondence of $[011]_{\alpha''M}//[100]_{\alpha''V}$ (Table. 4) and a common $(351)_{\alpha''}$ pole, the OR

4 between M1 and V2 is identified as "$\{351\}$"$<\bar{2}11>_{\alpha''}$ type II twinning which explains

5 that the observed intersected $\{111\}_{\alpha''}$ type I and $\{011\}_{\alpha''}$ compound twins are

6 secondary twins activated within a primary SA "$\{351\}$"$<\bar{2}11>_{\alpha''}$ type II twinning.

7 According to Inamura et al.[41], when the principal transformation strain on the c-

8 axis of martensite is negative and smaller than -0.007, the $\{011\}_{\alpha''}$ compound

9 twinning is generally accepted as SA twinning. However, in specific cases (e.g., Ti-

10 11Mo, wt%[73]), the $\{011\}_{\alpha''}$ compound twinning with positive c-axis transformation

11 strain (η_3) was observed. Owing to the perfect lattice correspondence between the

12 $\{011\}_{\alpha''}$ compound twin and the well-known $\{0112\}_{\alpha}$ deformation twin in hcp α

13 structure, the $\{011\}_{\alpha''}$ compound twinning in such case is accepted as deformation

14 twinning[41]. This matches with our observation (Fig. 11) in which $\{011\}_{\alpha''}$ compound

15 twinning was observed in Ta13 whose c-axis transformation strain is also positive

16 (Table. 1), thereby the observed $\{011\}_{\alpha''}$ compound twinning being regarded as

17 mechanical twinning.
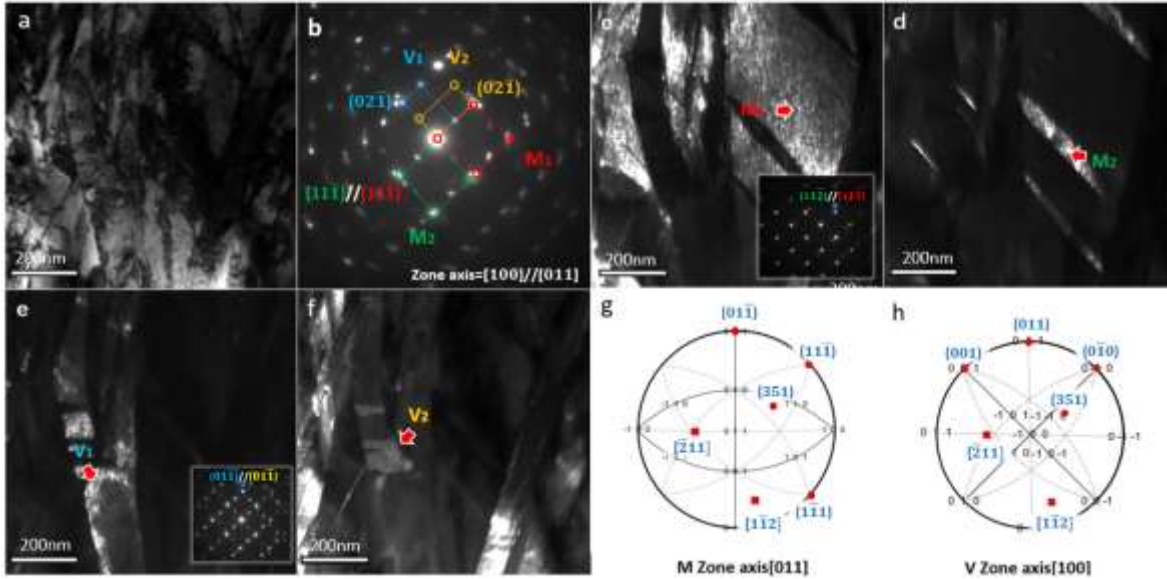
Fig. 11. TEM analysis of the microstructure in Ta13 with a strain of 20%. (a) BFI of the intersected deformation bands, (b) corresponding SADPs. DPs of four α'' martensite variants are marked by red, blue, green and yellow open circles, respectively. The variants are then divided into M and V groups for the $\{111\}_{\alpha''}$ and $\{011\}_{\alpha''}$ twinning related variants, respectively. (c-f) DFIs of the four α'' martensite variants. Insets in (c) and (e) are the corresponding SADPs of the twinning for M and V groups, respectively; (g, h) Stereographic projection figures constructed from crystallographic orientation taken from SADPs in (b).

4. Discussion

The present experimental results demonstrate that the impressive mechanical response of Ta13 is mainly attributed to the consistently dynamic refining effect associated with initial TRIP effect (β to α'') and the ensuing sequentially activated martensitic TWIP effect. The multi-stage hardening behavior is enabled through a special twinning transformation process which allows fine mechanical $\{351\}_{\alpha''}$ type I twinning to nucleate from primary SA "$\{351\}$"$<\bar{2}11>_{\alpha''}$ type II twinning. In the following, we mainly discuss the strengthening effect of this specific martensitic twinning

transformation induced strengthening mechanism as well as the activation

requirements for this martensitic type II to type I twinning transformation.

4.1. Strengthening mechanisms of martensitic twinning transformation

To illustrate the underlying strengthening behavior through the whole deformation

duration, Fig. 12a provides detailed information about the development of the

martensitic twinning transformation strengthening mechanism in Ta13. In stage I (0-

1.5%), a steep drop of work hardening is observed after yielding due to the transition

from elastic to plastic deformation where dislocation slip generally dominates the

initial plastic deformation in β phase[74]. With increasing strain, the β to α'' phase

transformation is activated. The elastic deformation in the yet formed α'' phase,

together with the increased density of phase boundaries, contribute to the work

hardening[75], thereby mitigating the drop of work hardening rate for Ta13 (8 GPa).

Analogous to TRIP Ti-alloys[25], further straining (stage II (1.5%-4%)) promotes the

martensitic transformation and primary martensite laths coarsening (Table. 2). To

accommodate the overall volume change during phase transformation, the

increased fraction of mechanically induced α'' phase in turn encourages two types

of α'' SA twinning (i.e., $\{111\}_{\alpha''}$ type I and $<\bar{2}11>_{\alpha''}$ type II twinning) nucleation within

β grain (Fig. 3) and the generation of one mechanical α'' twinning (i.e., $\{351\}_{\alpha''}$ type I

twinning). It is worth noting that, as identified by EBSD and TEM analysis, Figs. 3-7

provide solid evidence for the existence of a specific "$\{351\}$"$<\bar{2}11>_{\alpha''}$ type II twinning

mode which plays an essential role in the martensitic twinning transformation

mechanism. Meanwhile, as revealed by supplementary Fig. 1a and b, the

interactions between martensites and dislocations were observed by TEM analysis

in 3% strained Ta13 specimen, indicating that plastic deformation occurred in β phase of Ta13 during stage II. The synergetic effect of dynamic strengthening associated with SA martensitic twins and elastic deformation of the newly formed martensite in Ta13 dramatically contributes to the high work hardening rate of 12.5 GPa at ~4% strain during stage II, which notably outperforms that of other high-performance alloys[31,47–50] with work hardening rates of 2-4 GPa at similar strain levels. As the strain extends to stage III (4-6.5%), the strengthening effect arising from phase transformation tends to saturate and plastic deformation is prevalent in the martensite at this stage. Thus, the work hardening rate decreases gradually during stage III. Nevertheless, owing to the strong dynamic strengthening effect of martensitic transformation and the grain refinement effect of primary martensite laths by hierarchical submicron martensitic twins (refined average martensite size down to 0.67 µm for Ta13 at 6% strain), the work hardening rate of Ta13 remains as high as 5GPa at 6%. As revealed by Fig. 5, extensive SA twins suggest that besides the increased phase boundary density due to martensitic transformation, an increase of strain also encourages the formation of nano-scale secondary SA structures within the coarse SA twinned α'' variants. As the twinning boundaries are more effective in blocking dislocation motion than α''/β phase boundaries[76], the combination of copious $\{111\}_{\alpha''}$ and high index $\{351\}_{\alpha''}$ twinning boundaries provides major obstacles for dislocation movement, thus contributing to the high work hardening capability during the deformation of stage III. In most TRIP assisted alloys[29,77], further straining beyond the peaked work hardening rate would lead to a quick monotonous decrease of work hardening rate until failure due to the lack of an effective

1   strengthening mechanism. However, in stage IV (6.5%--12%) of our Ta13 alloy, the

2   decrease of work hardening rate is greatly alleviated and still maintained as high as

3   3~4 GPa. A distinct hump in the work hardening exponent curves is visible at the

4   onset of stage IV in Fig. 1c, indicating the activation of an additional deformation

5   mode. Without requiring additional displacive atomic shuffle that outside the twinning

6   shear plane to move one-half of the atoms to the appropriate twinned lattice sites,

7   the decrease of α'' mechanical twinning nucleation barrier greatly facilitates the

8   formation of the mechanical $\{351\}_{\alpha''}$ type I twins within primary SA type II

9   "{351}"$<\bar{2}11>_{\alpha''}$ twins at this stage (Fig. 10c). This novel transformation mechanism

10   enables the strengthening effect of martensitic mechanical twinning to be easily

11   introduced in an energetically favored route as illustrated in Fig. 12b. The resultant

12   nano-scale planar feature dramatically subdivides the width of primary martensite

13   plates down to nanometer scale, forming a hierarchal nanosized twinning structure.

14   This is essential to maintain the consistently high work hardening capability and

15   accommodate plastic deformation of the alloy[25,53,78–80], thereby contributing to

16   a work hardening rate as high as ～4GP at this high strain level. Moreover, the extra

17   shear that is required during the type II to type I twinning transformation process as

18   shown in Fig. 10c in turn accommodates the plastic deformation in martensite[81,82],

19   which contributes to the relaxation of local stress concentration.

20   After ~12% strain (stage V (12%-25%)), as expressed by the work hardening

21   exponent, n, the strengthening effect of Ta15 decreases until fracture (Fig. 1c),

22   whereas for Ta13, n increases from 0.22 to 0.31. The increase of n in Ta13 is

23   attributed to the activation of $\{011\}_{\alpha''}$ compound mechanical twins and secondary

$\{111\}_{\alpha''}$ twins in the primary SA type II "$\{351\}$"$<\bar{2}11>_{\alpha''}$ twins which results in the formation of intricate networks (Fig. 11), leading to consistently high work hardening in the late deformation stage of Ta13.

4.2. Critical conditions for activating martensitic twinning transformation

In the present work, the martensitic twinning transformation mechanism is believed to play a key role in maintaining the consistently high work hardening capability. Although similar near fully reorientated twinned variant has been captured in primary twinning of hexagonal alloys, such as Ti[83] and Mg[84] alloys, and known as double twinning, a twinning transformation that enabled a SA type II twinning to mechanical type I twinning transformation has not been reported. To better understand this mechanism and render martensitic twinning transformation being applicable to other alloy systems, two prerequisites that are essential for the activation of martensitic twinning transformation are identified: i, from the mechanical perspective, the TRIP induced volume change, which acts as the driving force for the early stage martensitic SA type II twins formation; ii, from crystallographic perspective, the SA type II twinning system should share the same twinning plane with an energetically favored (small twinning shear vector and simple atomic shuffle mechanism) mechanical type I twinning system to enable the type II to type I twinning transformation.

The first condition is easy to be satisfied in TRIP alloys, therefore emphasis is placed on the second condition. Similar to SA twins in many other TRIP alloys (i.e., Ti-Ni and Ti-Nb)[43], both the Bilby-Crocker deformation twinning theory[70] and infinitesimal deformation approach (IDA)[41,85] were employed to calculate the

transformable martensitic SA twinning modes in α''. Based on previous work which highlighted the importance of β phase stability and lattice parameters of α'' in SA twinning modes selection[41], in present work, the α'' martensite phase lattice parameter ratios, b/a and c/a, were taken as variables to calculate the transformable martensitic twinning modes (Fig. 12c). Three rational twinning plane solutions for the SA type II <$\bar{2}$11>$_{α''}$ twinning: Mode.1 {351}$_{α''}$, Mode.2 {131}$_{α''}$ and Mode.3 {111}$_{α''}$ are derived and listed in Table. 6 with their corresponding twinning elements. By comparing with possible mechanical twinning modes in α'' martensite that predicted by Tobe et al.[57] on a BCT structure that very close to the α'' structure, two most possible mechanical twinning modes {351}$_{α''}$ and {131}$_{α''}$ type I twins are screened and listed in Table. 6. However, it is needs to be noted that the shear vector 0.5407 of {351}$_{α''}$ type I twinning in Ta13 is different from 0.3536 as calculated by Tobe et al.[57], which is because the deviations of the lattice parameters from the ideal BCT structure to orthorhombic structure of α''.

**Table. 6**

Possible transformable α'' twinning modes with twinning elements and their lattice corresponding mechanical twinning modes. (The miller indices are rounded into integer for convenience)

Possible twinning modes	K_1	η_1	K_2	η_2	s
<$\bar{2}$11> type II Mode 1	{3$\bar{5}$$\bar{1}$}	<211>	{111}	<4$\bar{3}$$\bar{1}$>	0.0801
<$\bar{2}$11> type II Mode 2	{$\bar{1}$3$\bar{1}$}	<211>	{111}	<$\bar{2}$3$\bar{1}$>	0.1477
<$\bar{2}$11> type II Mode 3	{1$\bar{1}$$\bar{1}$}	<211>	{111}	<$\bar{2}$11>	0
{351}<1$\bar{1}$2> type I[57] Mode 1	{351}	<1$\bar{1}$2>	{1$\bar{1}$3}	<110>	0.3536
{131} type I[57] Mode 2	{131}	<$\bar{1}$01>	{$\bar{1}$13}	<110>	0.7071

*{351} type I Mode 1	{351}	$<\bar{1}\bar{1}8>$	{001}	<110>	0.5407

1 *Calculated with lattice parameter of α'' phase of Ta13

2 Based on the fact that the selection of SA type II $<\bar{2}11>_{\alpha''}$ twinning modes is

3 dependent on the c/a and b/a ratios of α'' as shown in Fig. 12c, it is pertinent to

4 deduce that the variation of c/a and b/a ratios which are both relevant to phase

5 stability[86] could encourage the SA $<\bar{2}11>_{\alpha''}$ type II twinning to select different

6 rational lattice planes as twinning plane. In our case, as the b/a and c/a ratios of α''

7 lattice for Ta13 (Fig. 12c) is close to the critical value for the activation of

8 "{351}"$<\bar{2}11>_{\alpha''}$ type II twinning, together with the smaller twinning shear vector of

9 {351}$_{\alpha''}$ type I twinning required for twinning transformation activation, the SA

10 "{351}"$<\bar{2}11>_{\alpha''}$ type II to mechanical {351}$_{\alpha''}$ type I twinning transformation occurred

11 extensively. Previous report on the observation of "{13$\bar{1}$}"$<\bar{2}11>_{\alpha''}$ type II twinning in

12 the Ti-20Nb alloy[87] also confirms that both the c/a and b/a ratios are critical for the

13 selection of specific SA type II $<\bar{2}11>_{\alpha''}$ twinning modes (Fig. 12c). However, as for

14 the "{13$\bar{1}$}"$<\bar{2}11>_{\alpha''}$ type II twinning observed in Ti-20Nb, the rather higher twinning

15 shear vector of 0.7071 in corresponding {13$\bar{1}$}$_{\alpha''}$ type I twinning (Table. 6) may

16 prevent the further transformation of "{13$\bar{1}$}"$<\bar{2}11>_{\alpha''}$ type II twinning, which explains

17 the absence of the martensitic twinning transformation effect in Ti-20Nb[87].
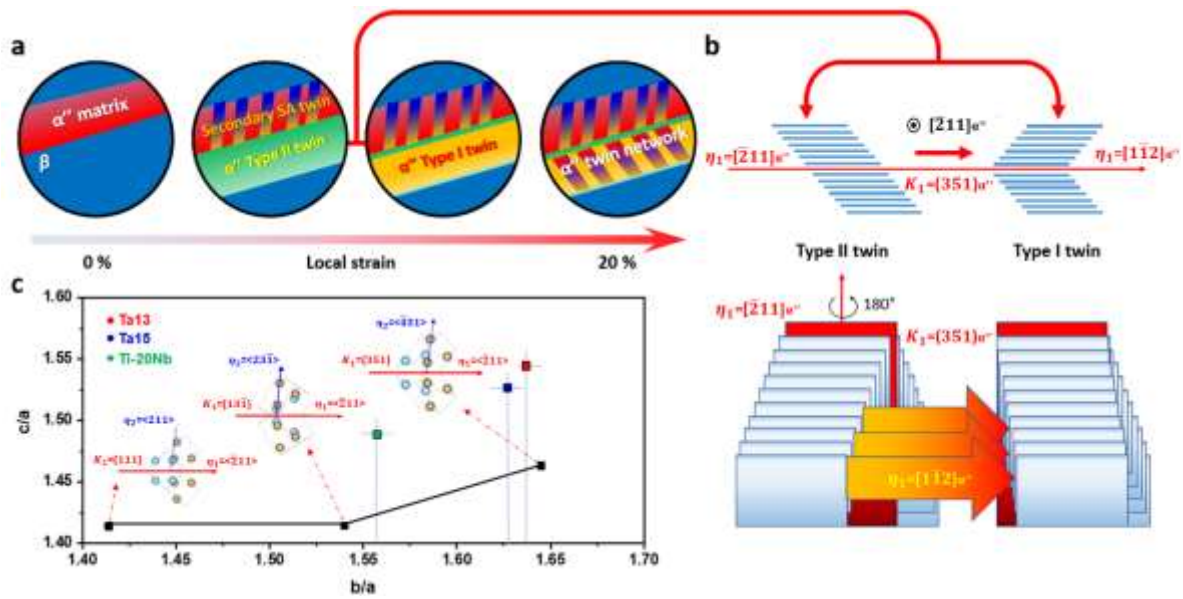
Fig. 12. Schematic illustration of (a) microstructural evolution and deformation mechanisms occurring during deformation and (b) schematic sketches illustrating the nucleation of mechanical $\{351\}_{\alpha''}$ type I twins within "$\{351\}$"$<\bar{2}11>_{\alpha''}$ type II twinned α'' variants. (c) The dependence of $<\bar{2}11>_{\alpha''}$ type II twinning mode selection on the c/a and b/a ratios. The critical c/a and b/a ratios for activation of three rational $<\bar{2}11>_{\alpha''}$ type II twinning modes are highlighted. The c/a and b/a ratios of Ta13, Ta15 and Ti-20Nb[87] are calculated and represented by red, blue and green squares, respectively.

Conclusions

In the present work, the innovative concept of martensitic twinning transformation strengthening mechanism is demonstrated experimentally and theoretically for the first time in metastable refractory BCC-HEAs. Tensile tests were conducted to induce the formation of stress-induced martensites, SA twinning and martensitic mechanical twinning in two carefully designed compositions Ta15 and Ta13. Phase transformation and plastic deformation yield intensive hierarchical martensitic SA and mechanical twins that significantly refined the primary

1   martensites were characterized and investigated via XRD, EBSD and TEM. On the

2   basis of experimental observations and calculations, we draw the following

3   conclusions:

4   ● The metastable BCC-HEAs Ta15 and Ta13 exhibit single β phase constitution

5   after carefully selected heat-treatment. During tensile deformation, Ta13 shows

6   considerable mechanical performance with a highlighted work hardening

7   sustainability in the range of 2-12.5 GPa, high tensile strength of 1.3 GPa and

8   large uniform elongation of 24%.

9   ● Activation of stress-induced martensite was observed during deformation for

10   both alloys. The lattice structure of the observed martensite is confirmed as

11   orthorhombic α''. Sequential activation of different α'' martensitic twinning

12   systems (including SA $\{111\}_{α''}$ type I, $\{011\}_{α''}$ mechanical twinning, newly

13   discovered SA "$\{351\}$"$<\bar{2}11>_{α''}$ type II and mechanical $\{351\}_{α''}$ type I twinning)

14   was observed that effectively sustained the high work hardening rate inherited

15   from TRIP effect at early stage to fracture.

16   ● A special α'' mechanical twinning nucleation route is reported for the first time

17   which simplifies the complex atomic shuffle for the direct activation of α''

18   mechanical twinning through nucleating the mechanical $\{351\}_{α''}$ type I twinning

19   within the primary SA "$\{351\}$"$<\bar{2}11>_{α''}$ type II twinned variant via simple shear.

20   Schmid analysis revealed that this martensitic twinning transformation behavior

21   obeys the Schmid law. Besides the promoted dynamic strengthening effect, the

22   extra shear that required during the type II to type I twinning transformation can

accommodate additional strain which further contributes to sustain the plastic deformation in martensite and relax local stress concentration.

- This martensitic twinning transformation strengthening mechanism bridges the gap between TRIP and TWIP effect via martensitic SA type II to mechanical type I twinning transformation and introduces a continuous strengthening source to maintain the high work hardening capability. The combination of IDA and deformation twinning analyses provides a solid rationale of the martensitic twinning transformation strengthening mechanism, which offers a new opportunity to introduce this mechanism into other β to α" TRIP alloys by adjusting the c/a and b/a ratios in α" phase.

CRediT authorship contribution statement

Yuhe Huang: Conceptualization, Methodology, Formal analysis, Writing - original draft. **Junheng Gao:** Methodology, Formal analysis, Writing - review & editing. **Vassili Vorontsov:** Methodology, Formal analysis, Writing - review & editing. **Dikai Guan:** Methodology, Formal analysis. **Russell Goodall:** Writing - review & editing. **David Dye**: Methodology. **Shuize Wang:** Validation. **Qiang Zhu:** Writing - review & editing. **W.Mark Rainforth:** Supervision, Writing - review & editing, Project administration, Funding acquisition. **Iain Todd:** Supervision, Writing - review & editing, Project administration, Funding acquisition.

References

[1]   B. Gludovatz, A. Hohenwarter, D. Catoor, E.H. Chang, E.P. George, R.O. Ritchie, A fracture-resistant high-entropy alloy for cryogenic applications, Science (80-.). (2014). https://doi.org/10.1126/science.1254581.

[2]   J.W. Yeh, S.K. Chen, S.J. Lin, J.Y. Gan, T.S. Chin, T.T. Shun, C.H. Tsau, S.Y. Chang, Nanostructured high-entropy alloys with multiple principal elements: Novel alloy design concepts and outcomes, Adv. Eng. Mater. (2004). https://doi.org/10.1002/adem.200300567.

[3]   Z. Lei, X. Liu, Y. Wu, H. Wang, S. Jiang, S. Wang, X. Hui, Y. Wu, B. Gault, P. Kontis, D. Raabe, L. Gu, Q. Zhang, H. Chen, H. Wang, J. Liu, K. An, Q. Zeng, T.G. Nieh, Z. Lu, Enhanced strength and ductility in a high-entropy alloy via ordered oxygen complexes, Nature. (2018). https://doi.org/10.1038/s41586-018-0685-y.

[4]   W. Lu, J. Li, Synergetic deformation mechanism in hierarchical twinned high-entropy alloys, J. Mater. Sci. \& Technol. 102 (2022) 80–88.

[5]   Z. An, S. Mao, Y. Liu, H. Zhou, Y. Zhai, Z. Tian, C. Liu, Z. Zhang, X. Han, Hierarchical grain size and nanotwin gradient microstructure for improved

mechanical properties of a non-equiatomic CoCrFeMnNi high-entropy alloy, J. Mater. Sci. \& Technol. 92 (2021) 195–207.

[6] O.N. Senkov, D.B. Miracle, K.J. Chaput, J.P. Couzinie, Development and exploration of refractory high entropy alloys - A review, J. Mater. Res. (2018). https://doi.org/10.1557/jmr.2018.153.

[7] C.C. Juan, M.H. Tsai, C.W. Tsai, C.M. Lin, W.R. Wang, C.C. Yang, S.K. Chen, S.J. Lin, J.W. Yeh, Enhanced mechanical properties of HfMoTaTiZr and HfMoNbTaTiZr refractory high-entropy alloys, Intermetallics. (2015). https://doi.org/10.1016/j.intermet.2015.03.013.

[8] Y.D. Wu, Y.H. Cai, T. Wang, J.J. Si, J. Zhu, Y.D. Wang, X.D. Hui, A refractory Hf 25 Nb 25 Ti 25 Zr 25 high-entropy alloy with excellent structural stability and tensile properties, Mater. Lett. (2014). https://doi.org/10.1016/j.matlet.2014.05.134.

[9] J. Chen, X. Zhou, W. Wang, B. Liu, Y. Lv, W. Yang, D. Xu, Y. Liu, A review on fundamental of high entropy alloys with promising high–temperature properties, J. Alloys Compd. (2018). https://doi.org/10.1016/j.jallcom.2018.05.067.

[10] M. Wu, S. Wang, F. Xiao, G. Zhu, C. Yang, D. Shu, B. Sun, Dislocation glide and mechanical twinning in a ductile VNbTi medium entropy alloy, J. Mater. Sci. \& Technol. (2021).

[11] Y. Cao, W. Zhang, B. Liu, Y. Liu, M. Du, A. Fu, Phase decomposition behavior and its effects on mechanical properties of TiNbTa0. 5ZrAl0. 5 refractory high entropy alloy, J. Mater. Sci. \& Technol. 66 (2021) 10–20.

[12] T. Xiang, Z. Cai, P. Du, K. Li, Z. Zhang, G. Xie, Dual phase equal-atomic NbTaTiZr high-entropy alloy with ultra-fine grain and excellent mechanical properties fabricated by spark plasma sintering, J. Mater. Sci. \& Technol. 90 (2021) 150–158.

[13] C. Lee, G. Song, M.C. Gao, R. Feng, P. Chen, J. Brechtl, Y. Chen, K. An, W. Guo, J.D. Poplawsky, S. Li, A.T. Samaei, W. Chen, A. Hu, H. Choo, P.K. Liaw, Lattice

distortion in a strong and ductile refractory high-entropy alloy, Acta Mater. 160

(2018) 158–172. https://doi.org/https://doi.org/10.1016/j.actamat.2018.08.053.

[14]   Z. An, S. Mao, Y. Liu, L. Wang, H. Zhou, B. Gan, Z. Zhang, X. Han, A novel

HfNbTaTiV high-entropy alloy of superior mechanical properties designed on the

principle of maximum lattice distortion, J. Mater. Sci. Technol. 79 (2021) 109–117.

https://doi.org/https://doi.org/10.1016/j.jmst.2020.10.073.

[15]   D.B. Miracle, O.N. Senkov, A critical review of high entropy alloys and related

concepts, Acta Mater. (2017). https://doi.org/10.1016/j.actamat.2016.08.081.

[16]   F. Maresca, W.A. Curtin, Mechanistic origin of high strength in refractory BCC high

entropy alloys up to 1900K, Acta Mater. (2020).

https://doi.org/10.1016/j.actamat.2019.10.015.

[17]   O.N. Senkov, G.B. Wilks, J.M. Scott, D.B. Miracle, Mechanical properties of

Nb25Mo25Ta25W25 and V20Nb20Mo20Ta20W20 refractory high entropy alloys,

Intermetallics. (2011). https://doi.org/10.1016/j.intermet.2011.01.004.

[18]   O.N. Senkov, S. V. Senkova, C. Woodward, Effect of aluminum on the

microstructure and properties of two refractory high-entropy alloys, Acta Mater.

(2014). https://doi.org/10.1016/j.actamat.2014.01.029.

[19]   Y. Zou, S. Maiti, W. Steurer, R. Spolenak, Size-dependent plasticity in an

Nb25Mo25Ta 25W25 refractory high-entropy alloy, Acta Mater. (2014).

https://doi.org/10.1016/j.actamat.2013.11.049.

[20]   O.N. Senkov, S. Gorsse, D.B. Miracle, High temperature strength of refractory

complex concentrated alloys, Acta Mater. (2019).

https://doi.org/10.1016/j.actamat.2019.06.032.

[21]   D.T. Pierce, J.A. Jiménez, J. Bentley, D. Raabe, C. Oskay, J.E. Wittig, The

influence of manganese content on the stacking fault and austenite/ε-martensite

interfacial energies in Fe-Mn-(Al-Si) steels investigated by experiment and theory, Acta Mater. (2014). https://doi.org/10.1016/j.actamat.2014.01.001.

[22] S. Turteltaub, A.S.J. Suiker, Transformation-induced plasticity in ferrous alloys, J. Mech. Phys. Solids. (2005). https://doi.org/10.1016/j.jmps.2005.03.004.

[23] M.M. Wang, C.C. Tasan, D. Ponge, A.C. Dippel, D. Raabe, Nanolaminate transformation-induced plasticity-twinning-induced plasticity steel with dynamic strain partitioning and enhanced damage resistance, Acta Mater. (2015). https://doi.org/10.1016/j.actamat.2014.11.010.

[24] J. Tran, Titanium by design: Trip titanium alloy, ProQuest Diss. Theses Glob. (2009).

[25] F. Sun, J.Y. Zhang, M. Marteleur, T. Gloriant, P. Vermaut, D. Laillé, P. Castany, C. Curfs, P.J. Jacques, F. Prima, Investigation of early stage deformation mechanisms in a metastable β titanium alloy showing combined twinning-induced plasticity and transformation-induced plasticity effects, Acta Mater. (2013). https://doi.org/10.1016/j.actamat.2013.07.019.

[26] F. Sun, J.Y. Zhang, C. Brozek, M. Marteleur, M. Veron, E. Rauch, T. Gloriant, P. Vermaut, C. Curfs, P.J. Jacques, F. Prima, The role of stress induced martensite in ductile metastable Beta Ti-alloys showing combined TRIP/TWIP Effects, Mater. Today Proc. (2015). https://doi.org/10.1016/j.matpr.2015.07.336.

[27] Q.Y. Sun, S.J. Song, R.H. Zhu, H.C. Gu, Toughening of titanium alloys by twinning and martensite transformation, J. Mater. Sci. (2002). https://doi.org/10.1023/A:1015456026919.

[28] M. Marteleur, F. Sun, T. Gloriant, P. Vermaut, P.J. Jacques, F. Prima, On the design of new β-metastable titanium alloys with improved work hardening rate thanks to simultaneous TRIP and TWIP effects, Scr. Mater. (2012). https://doi.org/10.1016/j.scriptamat.2012.01.049.

[29]   X. Ma, F. Li, J. Cao, J. Li, Z. Sun, G. Zhu, S. Zhou, Strain rate effects on tensile deformation behaviors of Ti-10V-2Fe-3Al alloy undergoing stress-induced martensitic transformation, Mater. Sci. Eng. A. (2018). https://doi.org/10.1016/j.msea.2017.10.057.

[30]   H. Huang, Y. Wu, J. He, H. Wang, X. Liu, K. An, W. Wu, Z. Lu, Phase-Transformation Ductilization of Brittle High-Entropy Alloys via Metastability Engineering, Adv. Mater. (2017). https://doi.org/10.1002/adma.201701678.

[31]   L. Lilensten, J.P. Couzinié, J. Bourgon, L. Perrière, G. Dirras, F. Prima, I. Guillot, Design and tensile properties of a bcc Ti-rich high-entropy alloy with transformation-induced plasticity, Mater. Res. Lett. (2017). https://doi.org/10.1080/21663831.2016.1221861.

[32]   L. Wang, C. Fu, Y. Wu, R. Li, Y. Wang, X. Hui, Ductile Ti-rich high-entropy alloy controlled by stress induced martensitic transformation and mechanical twinning, Mater. Sci. Eng. A. (2019). https://doi.org/10.1016/j.msea.2019.138147.

[33]   L. Wang, C. Fu, Y. Wu, R. Li, X. Hui, Y. Wang, Superelastic effect in Ti-rich high entropy alloys via stress-induced martensitic transformation, Scr. Mater. (2019). https://doi.org/10.1016/j.scriptamat.2018.10.035.

[34]   L. Wang, T. Cao, X. Liu, B. Wang, K. Jin, Y. Liang, L. Wang, F. Wang, Y. Ren, J. Liang, Y. Xue, A novel stress-induced martensitic transformation in a single-phase refractory high-entropy alloy, Scr. Mater. 189 (2020) 129–134. https://doi.org/10.1016/j.scriptamat.2020.08.013.

[35]   A. Ramalohary, P. Castany, P. Laheurte, F. Prima, T. Gloriant, Superelastic property induced by low-temperature heating of a shape memory Ti-24Nb-0.5Si biomedical alloy, Scr. Mater. (2014). https://doi.org/10.1016/j.scriptamat.2014.06.009.

1   [36]   H.Y. Kim, Y. Ikehara, J.I. Kim, H. Hosoda, S. Miyazaki, Martensitic transformation,

2   shape memory effect and superelasticity of Ti-Nb binary alloys, Acta Mater. (2006).

3   https://doi.org/10.1016/j.actamat.2006.01.019.

4   [37]   J.T. Benzing, W.A. Poling, D.T. Pierce, J. Bentley, K.O. Findley, D. Raabe, J.E.

5   Wittig, Effects of strain rate on mechanical properties and deformation behavior of

6   an austenitic Fe-25Mn-3Al-3Si TWIP-TRIP steel, Mater. Sci. Eng. A. (2018).

7   https://doi.org/10.1016/j.msea.2017.11.017.

8   [38]   Z. Li, C.C. Tasan, H. Springer, B. Gault, D. Raabe, Interstitial atoms enable joint

9   twinning and transformation induced plasticity in strong and ductile high-entropy

10   alloys, Sci. Rep. (2017). https://doi.org/10.1038/srep40704.

11   [39]   W. Lu, C.H. Liebscher, G. Dehm, D. Raabe, Z. Li, Bidirectional Transformation

12   Enables Hierarchical Nanolaminate Dual-Phase High-Entropy Alloys, Adv. Mater.

13   (2018). https://doi.org/10.1002/adma.201804727.

14   [40]   Z. Li, K.G. Pradeep, Y. Deng, D. Raabe, C.C. Tasan, Metastable high-entropy dual-

15   phase alloys overcome the strength-ductility trade-off, Nature. (2016).

16   https://doi.org/10.1038/nature17981.

17   [41]   T. Inamura, J.I. Kim, H.Y. Kim, H. Hosoda, K. Wakashima, S. Miyazaki,

18   Composition dependent crystallography of α″-martensite in Ti-Nb-based β-titanium

19   alloy, Philos. Mag. (2007). https://doi.org/10.1080/14786430601003874.

20   [42]   T. Inamura, H. Hosoda, H. Kanetaka, H.Y. Kim, S. Miyazaki, Self-accommodation

21   morphology in Ti-Nb-Al shape memory alloy, in: Mater. Sci. Forum, 2010.

22   https://doi.org/10.4028/www.scientific.net/MSF.654-656.2154.

23   [43]   K. Bhattacharya, Self-accommodation in martensite, Arch. Ration. Mech. Anal.

24   (1992). https://doi.org/10.1007/BF00375026.

1   [44]   P. Majumdar, S.B. Singh, M. Chakraborty, Elastic modulus of biomedical titanium

2   alloys by nano-indentation and ultrasonic techniques-A comparative study, Mater.

3   Sci. Eng. A. (2008). https://doi.org/10.1016/j.msea.2007.12.029.

4   [45]   Y. Ma, W. Song, W. Bleck, Investigation of the microstructure evolution in a Fe-

5   17Mn-1.5Al-0.3C steel via in situ synchrotron X-ray diffraction during a tensile test,

6   Materials (Basel). (2017). https://doi.org/10.3390/ma10101129.

7   [46]   O. Grässel, L. Krüger, G. Frommeyer, L.W. Meyer, High strength Fe-Mn-(Al, Si)

8   TRIP/TWIP steels development - properties - application, Int. J. Plast. (2000).

9   https://doi.org/10.1016/S0749-6419(00)00015-2.

10   [47]   C. Brozek, F. Sun, P. Vermaut, Y. Millet, A. Lenain, D. Embury, P.J. Jacques, F.

11   Prima, A β-titanium alloy with extra high strain-hardening rate: Design and

12   mechanical properties, Scr. Mater. (2016).

13   https://doi.org/10.1016/j.scriptamat.2015.11.020.

14   [48]   X. Ji, S. Emura, X. Min, K. Tsuchiya, Strain-rate effect on work-hardening behavior

15   in β-type Ti-10Mo-1Fe alloy with TWIP effect, Mater. Sci. Eng. A. (2017).

16   https://doi.org/10.1016/j.msea.2017.09.055.

17   [49]   F. Sun, J.Y. Zhang, M. Marteleur, C. Brozek, E.F. Rauch, M. Veron, P. Vermaut,

18   P.J. Jacques, F. Prima, A new titanium alloy with a combination of high strength,

19   high strain hardening and improved ductility, Scr. Mater. (2015).

20   https://doi.org/10.1016/j.scriptamat.2014.09.005.

21   [50]   M. Ahmed, D. Wexler, G. Casillas, O.M. Ivasishin, E. V. Pereloma, The influence of

22   β phase stability on deformation mode and compressive mechanical properties of

23   Ti-10V-3Fe-3Al alloy, Acta Mater. (2015).

24   https://doi.org/10.1016/j.actamat.2014.10.043.

25   [51]   H. Mecking, U.F. Kocks, Kinetics of flow and strain-hardening, Acta Metall. (1981).

26   https://doi.org/10.1016/0001-6160(81)90112-7.

1   [52]   O. Bouaziz, D. Barbier, J.D. Embury, G. Badinier, An extension of the Kocks-

2   Mecking model of work hardening to include kinematic hardening and its application

3   to solutes in ferrite, Philos. Mag. (2013).

4   https://doi.org/10.1080/14786435.2012.704419.

5   [53]   Y. Yang, P. Castany, Y.L. Hao, T. Gloriant, Plastic deformation via hierarchical

6   nano-sized martensitic twinning in the metastable β Ti-24Nb-4Zr-8Sn alloy, Acta

7   Mater. 194 (2020) 27–39. https://doi.org/10.1016/j.actamat.2020.04.021.

8   [54]   T. Yang, Y.L. Zhao, Y. Tong, Z.B. Jiao, J. Wei, J.X. Cai, X.D. Han, D. Chen, A. Hu,

9   J.J. Kai, K. Lu, Y. Liu, C.T. Liu, Multicomponent intermetallic nanoparticles and

10   superb mechanical behaviors of complex alloys, Science (80-.). (2018).

11   https://doi.org/10.1126/science.aas8815.

12   [55]   X. Zhang, W. Wang, J. Sun, Formation of {332} ⟨113⟩ βtwins from parent {130}

13   ⟨310⟩ α″plastic twins in a full α″ Ti-Nb alloy by annealing, Mater. Charact. (2018).

14   https://doi.org/10.1016/j.matchar.2018.09.034.

15   [56]   E. Bertrand, P. Castany, Y. Yang, E. Menou, T. Gloriant, Deformation twinning in

16   the full-α″ martensitic Ti-25Ta-20Nb shape memory alloy, Acta Mater. (2016).

17   https://doi.org/10.1016/j.actamat.2015.12.001.

18   [57]   H. Tobe, H.Y. Kim, T. Inamura, H. Hosoda, S. Miyazaki, Origin of {3 3 2} twinning in

19   metastable β-Ti alloys, Acta Mater. (2014).

20   https://doi.org/10.1016/j.actamat.2013.10.048.

21   [58]   A.G. Crocker, The crystallography of deformation twinning in alpha-uranium, J.

22   Nucl. Mater. 16 (1965) 306–326. https://doi.org/10.1016/0022-3115(65)90119-4.

23   [59]   Y. Zhang, Z. Li, C. Esling, J. Muller, X. Zhao, L. Zuo, A general method to determine

24   twinning elements, J. Appl. Cryst. 43 (2010) 1426–1430.

25   https://doi.org/10.1107/S0021889810037180.

1 [60] M. Niewczas, Lattice correspondence during twinning in hexagonal close-packed

2 crystals, Acta Mater. 58 (2010) 5848–5857.

3 https://doi.org/10.1016/j.actamat.2010.06.059.

4 [61] L.N. Brewer, D.P. Field, C.C. Merriman, Mapping and Assessing Plastic

5 Deformation Using EBSD, (2009) 251–262. https://doi.org/10.1007/978-0-387-

6 88136-2_18.

7 [62] H. Gao, Y. Huang, W.D. Nix, J.W. Hutchinson, Mechanism-based strain gradient

8 plasticity - I. Theory, J. Mech. Phys. Solids. (1999). https://doi.org/10.1016/S0022-

9 5096(98)00103-3.

10 [63] L.P. Kubin, A. Mortensen, Geometrically necessary dislocations and strain-gradient

11 plasticity: A few critical issues, Scr. Mater. (2003). https://doi.org/10.1016/S1359-

12 6462(02)00335-4.

13 [64] M.D. Vaudin, Pseudosymmetry in EBSD Patterns, Microsc. Microanal. (2005).

14 https://doi.org/10.1017/s1431927605500710.

15 [65] S. Lee, C. Park, J. Hong, J. taek Yeom, The Role of Nano-domains in {1–011}

16 Twinned Martensite in Metastable Titanium Alloys, Sci. Rep. (2018).

17 https://doi.org/10.1038/s41598-018-30059-8.

18 [66] T. Inamura, H. Hosoda, H. Young Kim, S. Miyazaki, Antiphase boundary-like

19 stacking fault in α″-martensite of disordered crystal structure in β-titanium shape

20 memory alloy, Philos. Mag. (2010). https://doi.org/10.1080/14786435.2010.489889.

21 [67] Y. Nii, T.H. Arima, H.Y. Kim, S. Miyazaki, Effect of randomness on ferroelastic

22 transitions: Disorder-induced hysteresis loop rounding in Ti-Nb-O martensitic alloy,

23 Phys. Rev. B - Condens. Matter Mater. Phys. (2010).

24 https://doi.org/10.1103/PhysRevB.82.214104.

25 [68] R.W. Cahn, Plastic deformation of alpha-uranium, Acta Metall. 1 (1953) 49,IN1,53-

26 52,IN5,70. https://doi.org/10.1016/0001-6160(53)90009-1.

[69] X. Ji, I. Gutierrez-Urrutia, S. Emura, T. Liu, T. Hara, X. Min, D. Ping, K. Tsuchiya, Twinning behavior of orthorhombic-α″ martensite in a Ti-7.5Mo alloy, Sci Technol Adv Mater. 20 (2019) 401–411. https://doi.org/10.1080/14686996.2019.1600201.

[70] B.A. Bilby, A.G. Crocker, The Theory of the Crystallography of Deformation Twinning, Proc. R. Soc. A Math. Phys. Eng. Sci. (1965). https://doi.org/10.1098/rspa.1965.0216.

[71] E. Bertrand, P. Castany, I. Péron, T. Gloriant, Twinning system selection in a metastable $β$-titanium alloy by Schmid factor analysis, Scr. Mater. 64 (2011) 1110–1113.

[72] K. Bhattacharya, others, Microstructure of martensite: why it forms and how it gives rise to the shape-memory effect, Oxford University Press, 2003.

[73] S. Weinig, E.S. Machlin, Data for one of the martensitic transformations in an 11 pct Mo-Ti alloy, JOM. 6 (1954) 1280–1281.

[74] A. Rohatgi, K.S. Vecchio, G.T. Gray, The influence of stacking fault energy on the mechanical behavior of Cu and Cu-al alloys: Deformation twinning, work hardening, and dynamic recovery, Metall. Mater. Trans. A Phys. Metall. Mater. Sci. (2001). https://doi.org/10.1007/s11661-001-0109-7.

[75] T. Yoneyama, S. Miyazaki, Shape Memory Alloys for Biomedical Applications, 2008. https://doi.org/10.1533/9781845695248.

[76] M.J. Lai, C.C. Tasan, D. Raabe, On the mechanism of {332} twinning in metastable β titanium alloys, Acta Mater. (2016). https://doi.org/10.1016/j.actamat.2016.03.040.

[77] J. Shi, X. Sun, M. Wang, W. Hui, H. Dong, W. Cao, Enhanced work-hardening behavior and mechanical properties in ultrafine-grained steels with large-fractioned metastable austenite, Scr. Mater. (2010). https://doi.org/10.1016/j.scriptamat.2010.06.023.

[78] J. Gao, Y. Huang, D. Guan, A.J. Knowles, L. Ma, D. Dye, W.M. Rainforth, Deformation mechanisms in a metastable beta titanium twinning induced plasticity alloy with high yield strength and high strain hardening rate, Acta Mater. (2018). https://doi.org/10.1016/j.actamat.2018.04.035.

[79] K. Lu, L. Lu, S. Suresh, Strengthening materials by engineering coherent internal boundaries at the nanoscale, Science (80-.). (2009). https://doi.org/10.1126/science.1159610.

[80] J. Gao, S. Jiang, H. Zhang, Y. Huang, D. Guan, Y. Xu, S. Guan, L.A. Bendersky, A. V Davydov, Y. Wu, others, Facile route to bulk ultrafine-grain steels for high strength and ductility, Nature. 590 (2021) 262–267.

[81] S. Mahajan, D.F. Williams, Deformation Twinning in Metals and Alloys, Int. Metall. Rev. 18 (1973) 43–61. https://doi.org/10.1179/imtlr.1973.18.2.43.

[82] M.J. Lai, T. Li, D. Raabe, ω phase acts as a switch between dislocation channeling and joint twinning- and transformation-induced plasticity in a metastable β titanium alloy, Acta Mater. (2018). https://doi.org/10.1016/j.actamat.2018.03.053.

[83] S. Xu, M. Gong, Y. Jiang, C. Schuman, J.-S. Lecomte, J. Wang, Secondary twin variant selection in four types of double twins in titanium, Acta Mater. 152 (2018) 58–76. https://doi.org/https://doi.org/10.1016/j.actamat.2018.03.068.

[84] A.G. Crocker, Double twinning, Philos. Mag. 7 (1962) 1901–1924.

[85] Y. Liang, H. Kato, M. Taya, T. Mori, Infinitesimal approach to the crystallography of martensitic transformation: application to Ni-Ti, Scr. Mater. (2000). https://doi.org/10.1016/S1359-6462(00)00465-6.

[86] M. Bönisch, M. Calin, L. Giebeler, A. Helth, A. Gebert, W. Skrotzki, J. Eckert, Composition-dependent magnitude of atomic shuffles in Ti-Nb martensites, J. Appl. Crystallogr. (2014). https://doi.org/10.1107/S1600576714012576.

1 [87] H. Tobe, H.Y. Kim, T. Inamura, H. Hosoda, T.H. Nam, S. Miyazaki, Effect of Nb

2 content on deformation behavior and shape memory properties of Ti-Nb alloys, J.

3 Alloys Compd. (2013). https://doi.org/10.1016/j.jallcom.2012.02.023.

4

Supplementary material

6
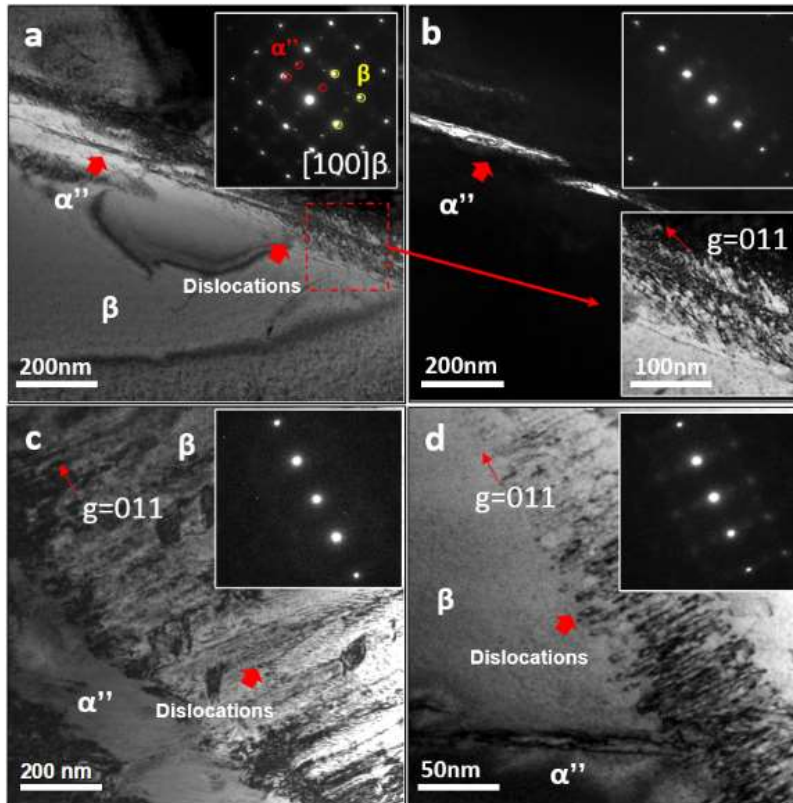
Supplementary Figure. 1 TEM images of 3% strained Ta13. (a) BFI imaged along the [100]$_\beta$ zone axis, inset is the corresponding SADPs. (b) DFI of the stress-induced martensite, insets are the corresponding SADPs, and dislocations imaged using g*=011. (c, d) Two-beam BFIs obtained from same sample, insets are the corresponding SADPs.